

The Pennsylvania State University
The Graduate School
College of Earth and Mineral Sciences

A RECORD OF COUPLED HILLSLOPE AND CHANNEL RESPONSE TO
PLEISTOCENE PERIGLACIAL EROSION IN A SANDSTONE HEADWATER
VALLEY, CENTRAL PENNSYLVANIA

A Thesis in
Geosciences
by
Joanmarie Del Vecchio

© 2017 Joanmarie Del Vecchio

Submitted in Partial Fulfillment
of the Requirements
for the Degree of

Master of Science

December 2017

The thesis of Joanmarie Del Vecchio was reviewed and approved* by the following:

Roman A. DiBiase
Assistant Professor of Geosciences
Thesis Advisor

Li Li
Associate Professor of Civil and Environmental Engineering

Susan L. Brantley
Professor of Geosciences

Tim Bralower
Professor of Geosciences
Interim Head, Department of Geosciences

*Signatures are on file in the Graduate School.

Abstract

Outside of the Last Glacial Maximum ice extent, landscapes in the central Valley and Ridge physiographic province of Appalachia preserve soils and thick colluvial deposits indicating extensive periglacial landscape modification. The preservation of periglacial landforms in the present interglacial suggests active hillslope sediment transport in cold climates followed by limited modification in the Holocene. However, the timing and extent of these processes are poorly constrained, and it is unclear whether, and how much, this signature is due to LGM or older periglacialiations. Here, we pair geomorphic mapping with in situ cosmogenic ^{10}Be and ^{26}Al measurements of surface material and buried clasts to estimate the residence time and depositional history of colluvium within Garner Run, a 1 km^2 sandstone headwater valley in central Appalachia containing relict Pleistocene periglacial features including solifluction lobes, boulder fields, and thick colluvial footslope deposits. ^{10}Be concentrations of stream sediment and hillslope regolith indicate slow erosion rates ($6.3\text{ m} \pm 0.5\text{ m.y.}^{-1}$) over the past 38-140 kyr. From dating of buried valley-bottom deposits recovered from a 9 m drill core, we interpret two depositional pulses since $\sim 290\text{ ka}$, a record which spans at least three glacial terminations and implies limited removal of valley bottom deposits during interglacials. This age is consistent with independent calculations determined from debris volume estimates, total hillslope contributing area, and catchment erosion rate integrated over multiple climate cycles. Thus, we infer that erosion rates measured in upland basins in Central Appalachia reflect the integration both temperate and periglacial processes, and that in cold-warm transitions, erosion rates reflect only moderate departures from otherwise slow background rates. Furthermore, due to slow erosion rates, we show that sedimentary records in sandstone headwater valleys present opportunities for direct examination of climate-modulated hillslope processes.

TABLE OF CONTENTS

LIST OF FIGURES	v
LIST OF TABLES	vi
ACKNOWLEDGEMENTS	vii
INTRODUCTION	1
STUDY AREA	2
METHODS	7
Topographic Analysis	7
Field Mapping of Regolith Texture	7
Grain Size Analysis of Surface Clasts on Hillslope and in Channels.....	8
Cosmogenic Nuclide Analysis.....	11
Determining Colluvial Fill History.....	13
RESULTS	14
Topographic Analysis	14
Field Mapping of Regolith Texture	15
Grain Size Analysis of Surface Clasts and Hillslopes and in Channels	16
Cosmogenic Nuclide Analysis.....	21
Constraining Colluvial Fill History	21
DISCUSSION	26
Controls on Spatial Variability in Regolith Texture and Morphology	26
Colluvial Fill History and Implications for Hillslope-Channel Coupling	30
Implications for the Evolution of the Critical Zone.....	33
CONCLUSIONS.....	34
References.....	36
Appendix A: Workflow of GPS-assisted soil mapping at Garner Run	41
Appendix B. Soil pit descriptions	45
Appendix C. Modeling Scenarios and Constants	52
Appendix Tables	55
Appendix Figures.....	58

LIST OF FIGURES

Figure 1. Study site in central Pennsylvania (p. 10)

Figure 2. Field photos showing heterogeneity in surface cover (p. 16)

Figure 3. Clast measurements from point counts conducted on hillslopes and in the channel (p. 24)

Figure 4. Shaded-relief models of colluvium (p. 25)

Figure 5. Summary of ^{10}Be concentrations in samples (p. 26)

Figure 6. Core samples taken from within the HV1 core (p. 29)

Figure 7. Forward-model outputs simulating deposition of debris recovered from valley core (p. 32)

Figure 8. Schematic diagram of geomorphology at the surface and subsurface at Garner Run (p. 34)

LIST OF TABLES

Table 1. Table 1: ^{10}Be and ^{26}Al data for all samples (p. 30)

ACKNOWLEDGEMENTS

This document is modified from a manuscript in preparation as of May 31, 2017 written with input from Paul Bierman and Alison Denn, including surface cosmogenic samples from Al. Field data collected and compiled with assistance of S. Granke, C. Martin and P. Silverhart. Funds for cosmogenic work provided by the Marie Morisawa Research Award through GSA's Quaternary Geology and Geomorphology Division. LiDAR data collection was funded by the National Science Foundation (NSF) and performed by the National Center for Airborne Laser Mapping (NCALM). Financial and logistical support were provided by the NSF-supported Susquehanna Shale Hills Critical Zone Observatory EAR – 1331726. This research was conducted in Rothrock State Forest which is funded and managed by the Pennsylvania Department of Conservation and Natural Resources, Bureau of Forestry. G. Mount, J. Hayes, X. Comas, F. Zarif, L. Guo, D. J. Merritts, F. J. Pazzaglia, B. Hoagland, V. Marcon and others provided thoughtful discussion. I would like to thank my geoscience classmates and intramural sports teammates for being a source of inspiration, enthusiasm and friendship. I thank my committee members, Susan L. Brantley and Li Li, for thought-provoking questions over the last two years, and I thank my advisor, Roman A. DiBiase, for his wonderful mentorship and encouragement as I began my journey in graduate school.

INTRODUCTION

Quaternary climate fluctuations profoundly influenced the style and pace of erosion in glaciated landscapes (Hallet et al., 1996; Koppes and Montgomery, 2009), but the extent to which erosion rates in nearby periglacial landscapes were affected by concurrent changes in temperature and hydrology remains unclear. While a switch to colder temperatures is thought to stimulate bedrock lowering through increased frost cracking (Hales and Roering, 2007; Anderson et al., 2013; Rempel et al., 2017), downslope transport of regolith by ice-driven creep, solifluction, and permafrost-thaw mass wasting is more efficient during transitional warming periods (Taber, 1929; Matsuoka, 2001; Lewkowitz and Harris, 2005). Additionally, headwater channel networks may be periodically overwhelmed by periglacial hillslope sediment flux (Pizzuto, 1995; Simpson and Schlunegger, 2003), insulating hillslopes from regional base level change and thus complicating the overall landscape response to changing climate.

In landscapes where erosion rates are slow compared to the frequency of climate shifts, weathering profiles within regolith integrate the effects of multiple glacial-interglacial cycles (Yoo et al., 2011; Anderson et al., 2013). In central Appalachia, the periglacial debris mantling hillslopes and valley floors is commonly assumed to reflect a single cold climate cycle experiencing re-equilibration in a temperate climate (Braun, 1989). However, the persistence of these relict landscape features alludes to a more complex history of sediment transport and coupled hillslope-channel responses. Periglacial landscapes like those in central Appalachia were common throughout middle latitudes during glacial periods (Vandenberghe et al., 2014). Thus, understanding how past environmental conditions control the composition and structure of the modern surface and shallow subsurface (Earth's "critical zone"), as well as the steadiness of

surface processes through time and space has wide applicability (Anderson et al., 2007; Brantley and Lebedeva, 2011).

In this study, we seek to understand the timescale, mechanisms, and extent of periglacial landscape modification by studying sediment stored in a headwater valley in central Pennsylvania. We quantify spatial variation in periglacial colluvium through detailed regolith mapping supplemented by analysis of lidar-derived high-resolution topography. We use the size, shape, and distribution of boulder colluvium on hillslopes and sediment in channels to infer sediment transport processes. To quantify erosion rates and patterns of hillslope sediment transport, we measure in-situ cosmogenic nuclide concentrations in regolith and stream sediment. We also measure in-situ cosmogenic ^{26}Al and ^{10}Be in a valley-bottom core to explore the timescale over which material derived from periglacial hillslope erosion is accumulated in the valley bottom. We then discuss implications of timescales of colluvium storage for the long-term evolution of headwater valleys and channels.

STUDY AREA

We focus on Garner Run, a 1 km² catchment underlain by the Silurian Tuscarora Formation within the Susquehanna Shale Hills Critical Zone Observatory (SSHCZO) in central Pennsylvania (Fig. 1a) (Brantley et al., 2016). The 150 m thick Tuscarora Formation is an orthoquartzite sandstone with minor thin interbedded olive-gray shale, and is overlain in some locations by an upper Castanea Member, an iron-cemented sandstone approximately 30 m thick (Flueckinger, 1969). Throughout central Pennsylvania, Paleozoic structures exhibit first order control on topography; the erosion-resistant Tuscarora Formation forms long linear ridges along plunging folds, which typically support the highest topography in the Valley and Ridge province (Fig. 1a).

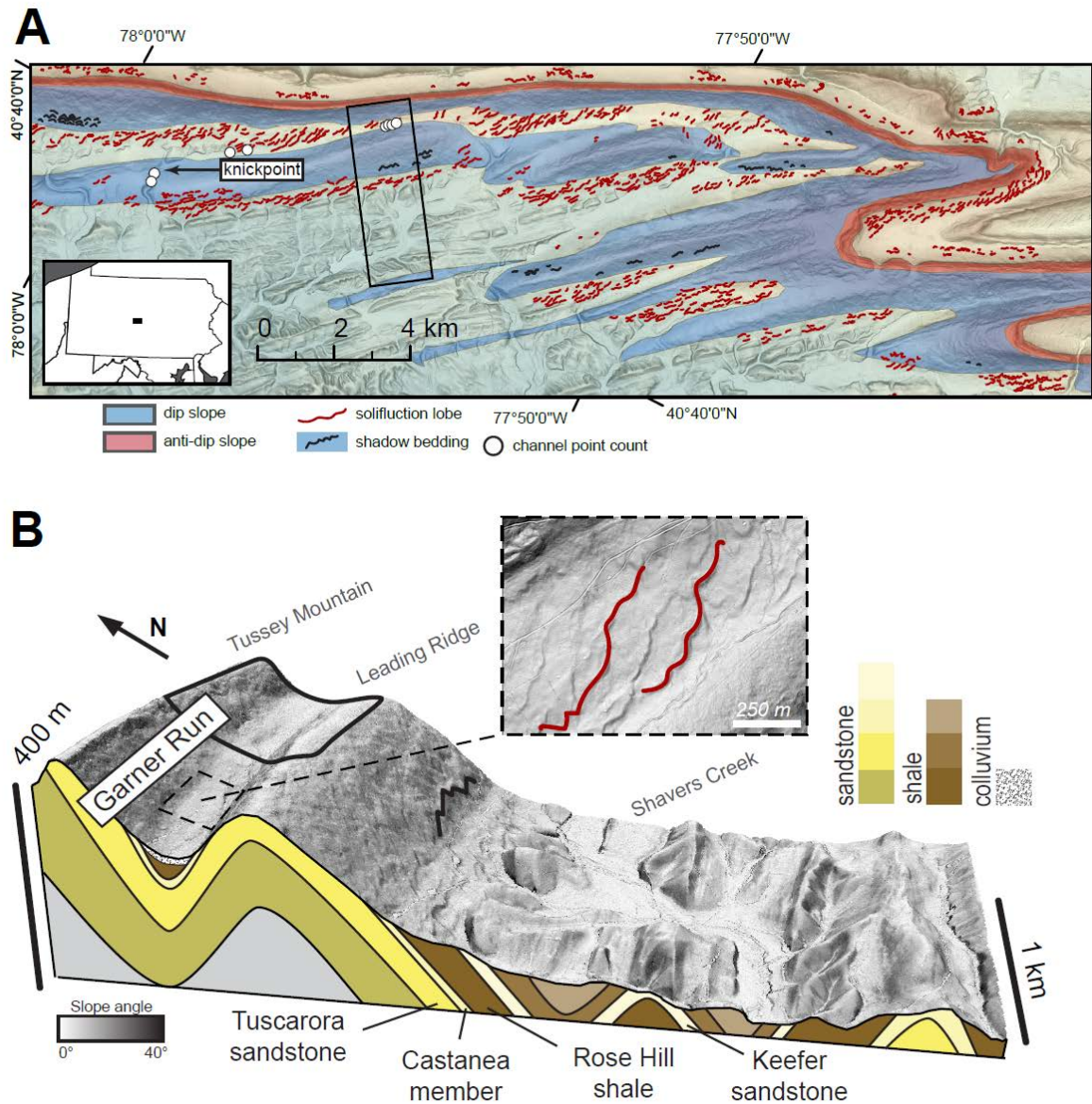


Fig. 1: (A) The topography of the Valley and Ridge physiographic province is marked by tight folds of resistant lithologies and valleys of erodible units like shale. On resistant lithologies, hillslope angles are controlled by underlying bedrock dip on dip slopes (blue polygons). Draped over these hillslopes are landscape features that indicate mass movement - solifluction lobes (red outlines) are thought to indicate periglacial sediment transport, subtle cuestas which we interpret to be shadow bedding (black outlines) indicate influence of bedrock dip under soil mantle. Garner Run contains a steepened river reach known as a knickpoint as it flows over a resistant anticline. Study site and the area shown in cross-section (Figure 1B) are located in the black box. Point count locations referenced in Fig. 3 are shown as white dots along the channel. (B) Perspective view of slope-shade maps of the Garner Run subcatchment along with the adjacent Shavers Creek, a tributary to the Susquehanna River. Underlying geologic cross-section shows Garner Run contained within Tuscarora syncline; the Leading Ridge ridgeline is a local anticline, while Tussey Mountain is a breached anticline. We show colluvium mantling the

bedrock in the valley at Garner Run, shadow bedding on Leading Ridge (also outlined in black) and slopeshade lidar imagery showing details of solifluction lobes in the valley (also outlined in red).

The Garner Run watershed lies within a synclinal valley bounded by two linear ridgelines—Tussey Mountain to the northwest, and Leading Ridge to the southeast—and the dip of the Tuscarora Formation parallels, or is slightly steeper than, hillslope topography (Flueckinger 1969). Further downvalley from the study catchment, the overlying Rose Hill Shale and the Keefer Sandstone crop out in the valley axis (Fig. 1b).

Overprinting the lithologic and structural control on topography in central Pennsylvania are patterns in bedrock river steepness and contrasting erosion rates above and below oversteepened river reaches known as knickpoints (Whipple and Tucker, 1999). Such disequilibria in river networks have been used to argue for a regional increase in the rate of base level fall that has propagated throughout the Susquehanna River basin since the Miocene (Miller et al., 2013). Downstream of the study catchment, Garner Run steepens at an elevation concurrent with the expected location of such a signal, but is also coincident with a lithologic and structural contrast across a Tuscarora anticline, where intact sandstone bedrock is exposed in the channel bed (Brantley et al., 2016), obscuring the degree to which this knickpoint reflects lithologic and/or base level change. At the original Shale Hills site, downstream of a knickpoint at a similar elevation, erosion rates are 15 m m.y.^{-1} (West et al., 2013); thus we expect erosion rates at Garner Run to be lower (Brantley et al., 2016).

Garner Run is located ~75 km south of the Last Glacial Maximum (LGM) extent at 25 ka (Corbett et al., 2017b) and till deposits indicate that glacial advances remained north of the area in both the Illinoian (~130 ka) and early Pleistocene (~800 ka) glaciations (Ramage et al., 1998; Ciolkosz et al., 2008). In northeastern North America, a cold-climate vegetation assemblage (spruce, fir and pines) dominated until the end of the Younger Dryas ~ 11 ka, at which point the modern suite of Holocene vegetation (temperate deciduous and warm mixed forests) was

established and persisted (Shuman, 2002; Williams et al., 2004). Palynological evidence indicates that tundra flora, perhaps in soils underlain by discontinuous or isolated permafrost, persisted in the central Valley and Ridge until ~16 ka, followed by a transitional period toward alpine communities until they were replaced by the modern hardwood community by 10 ka (Kneller and Peteet, 1999), though cold-climate vegetation communities may have endured longer at higher elevations (Kovar, 1965; Watts, 1979). Peak Holocene summer temperatures did not occur until 7 ka, corresponding to the weakening influence of the receding continental ice sheet and the thermal effects of summer insolation anomalies (Shuman and Marsicek, 2016). The modern climate of Garner Run is temperate (mean annual temperature of 10° C) with mean annual precipitation of 1.0 m (Thomas et al., 2013). Vegetation is characterized by deciduous trees with a few pines and hemlocks on ridgelines, though the area has been deforested a number of times since European settlement in the 18th century (Robinson, 1959).

Like other landscapes in the region, the Garner Run catchment bears evidence of extensive periglacial landscape modification as a consequence of colder temperatures in the Pleistocene. Boulder fields and landforms indicative of mass wasting processes are scattered across hillslopes at Garner Run (Fig. 2a). In the valley axis of Garner Run a broad, low-sloping bench with subtle lobate terraces hints at significant accumulation of colluvial deposits from adjacent hillslopes (Brantley et al. 2016). Throughout central Appalachia, colluvial deposits indicative of periglacial erosion blanket hillslopes and valley bottoms with blocky debris in resistant sandstone lithologies (Clark et al., 1992), influencing soils and hillslope morphology (Clark and Ciolkosz, 1988; Braun, 1989) as well as fluvial incision (Pizzuto, 1995; Reusser et al., 2004). The preservation of relict landforms today suggests vigorous periglacial landscape modification (Braun, 1989) and inhibited modification and evacuation of hillslope debris by modern landscape processes. Additionally,

higher catchment-averaged erosion rates in the Susquehanna River Basin versus the Potomac River Basin to the south may reflect more intense periglacial erosion adjacent to the LGM ice margin (Portenga et al., 2017). However, both the timing of periglacial modification and extent of the landscape inheritance of Pleistocene cold-period conditions remain poorly constrained.

METHODS

Topographic Analysis

We used 1-m resolution lidar-derived topography from both the 2010 leaf-off SSHCZO lidar survey (OpenTopography, 2010) and the 2006 PAMAP lidar of Pennsylvania (PAMAP Program, 2006) to generate slopeshade maps for identifying periglacial landforms throughout the Garner Run study catchment and nearby landscape (Fig. 1a). We mapped lobate structures that we interpret as relict solifluction lobe crests, hummocky terrain and landslides that we interpret as relict permafrost thaw slumps, and faint cuestas that we interpret to reflect shadow bedding of the underlying sandstone bedrock. Additionally, we generated topographic cross-sections at Garner Run to estimate the orientation and thickness of the underlying folded bedrock and interpret the thickness of colluvial valley fill, which is additionally constrained by a 9 m core in the valley axis and shallow geophysical surveys (DiBiase et al., 2016).

Field Mapping of Regolith Texture

To characterize spatial variations in regolith surface texture, we mapped boulder density and canopy cover in the field using lidar-derived maps on a smartphone and sub-meter resolution Bluetooth GPS for positioning. We defined five mapping units based on bedrock exposure, soil and boulder cover, and tree canopy cover: (1) soil (<10% surface boulders), (2) boulders/soil (10-67% surface boulders, embedded in soil), (3) boulder fields with tree canopy (>67% surface

boulders not embedded in soil) (4) open boulder fields with no tree canopy, and (5) in place bedrock (Fig. 2a). These surface textures lie on a continuum; we distinguished between boulders/soil and boulder fields based on whether boulders wobbled underfoot when disturbed, a proxy for the amount of interstitial soil. We mapped at a resolution of 5 m, which was chosen to balance mapping speed and detail and generally reflects the minimum scale over which regolith texture varies. We also dug several shallow (<1.5 m) soil pits on the different mapping units to examine clasts at depth, as well as their relation to any soil horizons.

Grain Size Analysis of Surface Clasts on Hillslope and in Channels

We conducted Wolman (1954) point counts of the intermediate axis of 40-100 surface clasts of at least cobble size (≥ 6.4 cm) along a 1 m grid at 20 hillslope sites to characterize surface patterns in grain size distribution. Hillslope sites included all mapped units except for fully soil mantled areas with no coarse surface clasts. Both open and canopied boulder fields typically contained no finer-grained material, and thus point counts reflect the full grain size distribution of regolith. Point counts of coarse sediment on otherwise soil-mantled surfaces (“boulders/soil” mapping classification) are not directly comparable, but provide constraints on the maximum boulder size.

At 8 locations along the channel, we conducted similar point counts, but incorporated all grains, defining material with diameter < 2 mm as “fine”. Four channel point counts were spaced approximately every 100 m in the headwaters, two point counts were conducted 4 km downstream from the subcatchment outlet, and two point counts were conducted 6 km downstream from the subcatchment outlet, where Garner Run turns southeast and steepens across a knickpoint (Brantley et al., 2016).

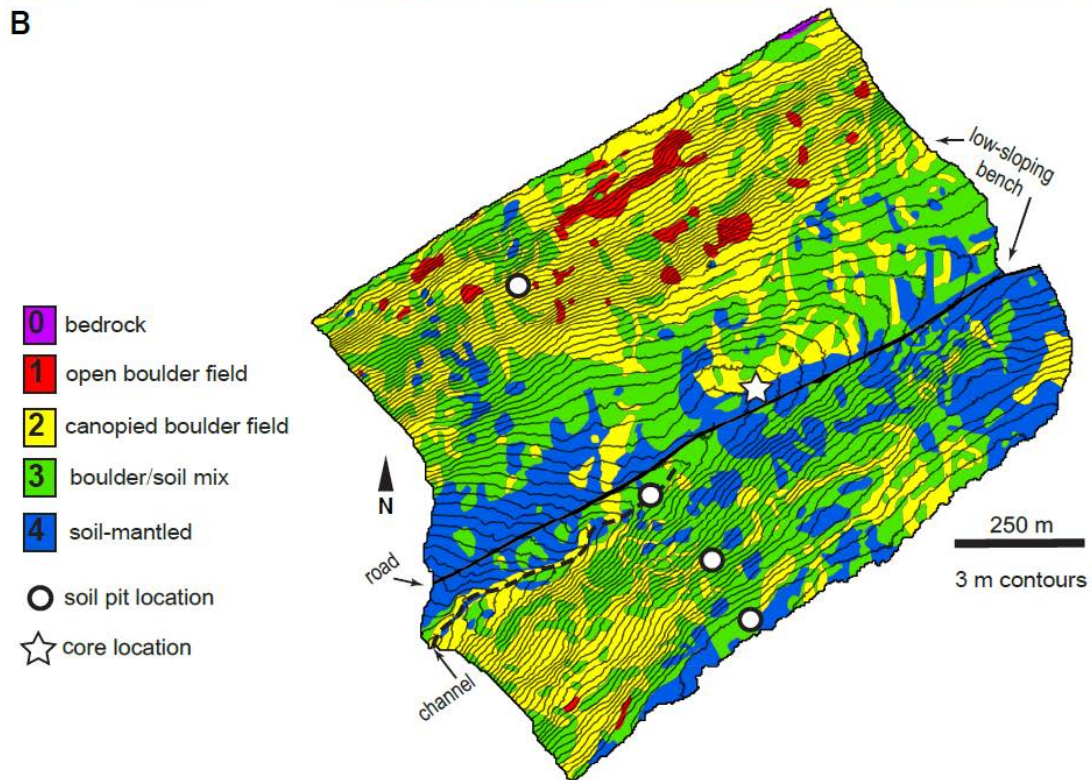
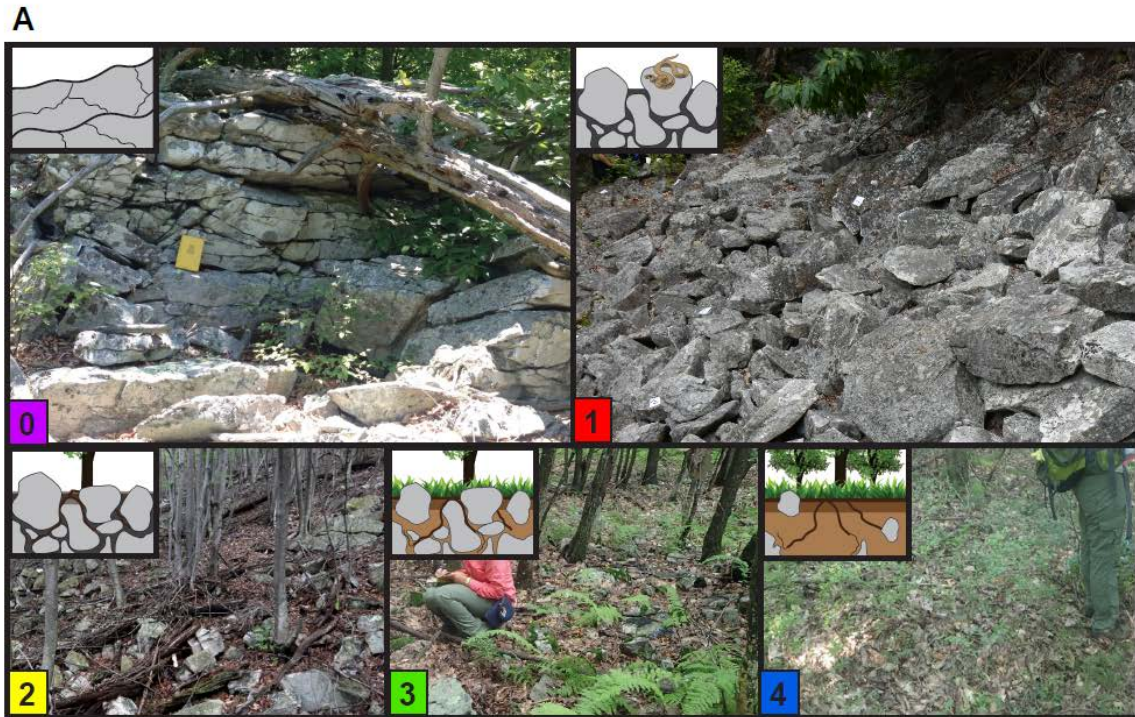


Fig. 2: (A) Field photos showing heterogeneity in surface cover. (0) Tuscarora sandstone cropping out at ridgeline, with primary horizontal fracturing along bedding planes. (1) Blockfields with large, debris are devoid of soil and prevent canopy growth. (2) Slopes with blocky debris but also patchy soils and trees. (3) Boulders with interstitial soil, and frequent

shrubs and other vegetation. (4) Soil mantled cover with few or no boulders. (B) Soil mapping results from the Garner Run subcatchment at 5m resolution. Contours highlight low slope of valley floor and relative steepness of adjacent hillslopes. Generally, more soil is located in the valley bottom, while nearer to ridgelines boulders are more prominent. Open blockfields are almost exclusively located on the south-facing slope, though rockiness tends to increase with distance down-valley on the north-facing Leading Ridge slope, where underlying bedrock dip steepens.

To aid in visualization of grain shape, sorting, and organization, we constructed structure-from-motion photogrammetry models (Westoby et al., 2012) of three point-count sites using a digital single lens reflex camera with wide angle lens. We aligned 50-100 photographs of each site and constructed dense point clouds using Agisoft Photoscan, and scaled our models using 3-5 15 cm rulers scattered throughout the scene. Visualization of dense point clouds was performed using the EyeDome lighting shader in CloudCompare (<http://danielgm.net/cc>).

Cosmogenic Nuclide Analysis

To quantify the concentration of cosmogenic nuclides in regolith, we sampled material from a soil pit transect established at Garner Run as part of the larger SSHCZO investigation known as the GroundHOG (three along the north-facing slope of Leading Ridge and one on the south-facing slope of Tussey Mountain, Fig. 2b) (Brantley et al., 2016). These pits were dug to different depths – to 0.7 m on the Tussey Mountain Midslope (TMMS), to 0.65 m on the Leading Ridge Ridgetop (LRRT), to 1.4 m on the Leading Ridge Midslope (LRMS), and to 1.4 m on the Leading Ridge Valley Floor (LRVF) – based on the depth of refusal and thus integrates only a portion of the regolith overlying unweathered bedrock. We amalgamated 100 g of soil from each soil horizon identified for a given soil pit, and sieved amalgamated horizon material to the 250-850 μm fraction sampled within the soil profile, creating a single sample for each soil pit.

We sampled surface boulders along three 30 m slope-normal transects adjacent to each of the three soil pits on the north-facing slope of Leading Ridge for both ^{10}Be and ^{26}Al (Fig. 2b). Every two meters we removed the uppermost few centimeters of rock from the nearest boulder, sampling boulders representative of the typical boulder size on the slope (~1 m or less) for a total of 15 boulder chips per transect. Each chip was crushed and sieved individually, and 50 g of each clast was amalgamated into one sample per transect. We collected fluvial sediments ~15 m

upstream and downstream from the north-facing soil transect, and sieved each sample in the field to the 250-850 μm fraction.

We sampled buried clasts recovered from a 9.1 m drill core in the valley axis of Garner Run, just upstream of the soil pit transect (Brantley et al., 2016; DiBiase et al., 2016). Material recovered during drilling consisted of discontinuous sandstone clasts dispersed throughout Fe-stained sandy fill. Two sandstone clasts were recovered between 0-3.3 m but their depths were not recorded. Five clasts between 3.4 and 4.8 m were recovered as were four clasts between 4.8 and 6.4 m; while their precise depths are unknown, the order of their recovery was noted, as was the length of each cored section. Sand was present between depths of 6.4 and 9.1 m, with no clasts. We sampled the first clast recovered in the 3.4-4.8 m interval as well as the first and last clast recovered from the 4.8-6.4 m interval to analyze both ^{26}Al and ^{10}Be to determine burial age and history (Granger, 2006). Because the drill casings were each 1.5 meters long, and cores were logged in the order they were recovered (rather than at discrete depths), there is some uncertainty in the depths of the individual clasts. The total length of cored clasts in the 3.4-4.8 interval was 0.38 m, and total length of cored clasts in the 4.8-6.4 interval was 0.45 m. We assigned a depth of 3.4, 4.8 and 6.4 to the top, middle and bottom clasts, respectively. However, the top and middle clasts may have been deeper and the bottom clast may have been shallower by as much as 0.5 m given the length of core recovered for each interval.

We purified quartz by heating ground samples in HCl and treating them with a series of leaches using dilute HF/HNO₃ mixtures at the University of Vermont (Kohl and Nishiizumi, 1992) and extracted ^{10}Be and ^{26}Al following the methods of Corbett et al. (2016a). All Garner Run samples were analyzed for ^{10}Be at Lawrence Livermore National Laboratory normalizing them relative to ICN standard 07KNSTD3110 with an assumed value of 2.85×10^{-12} (Nishiizumi et al.,

2007). Samples GR01-GR09 were analyzed in April 2016, and GR10-12 in July 2016. We corrected GR01-GR09 using an average of n=3 process blanks ($6.43 \pm 2.00 \times 10^{-16}$ atoms g⁻¹), and GR10-12 using an average of n=10 process blanks ($1.35 \pm 0.77 \times 10^{-15}$ atoms g⁻¹). We sent the drill core samples (n=3) and the surface boulder transect samples (n=3) to PRIME lab (n=6) for ²⁶Al analysis. Exposure ages were calculated using the CRONUS-Earth online calculator (<http://hess.ess.washington.edu/>, wrapper script 2.2, main calculator 2.1, constants 2.2.1, see Balco et al. (2008)) based on the constant production rate model (Lal, 1991; Stone, 2000) calibrated to the northeastern United States production rate (Balco et al., 2009)(Table A1). Two samples, GR08 and GR10, were replicated for ¹⁰Be and ²⁶Al measurements at PRIME lab in May 2017.

Determining Colluvial Fill History

As a first order constraint on the age of colluvial fill in Garner Run, we divided estimates of fill volume constrained by surface topography, drill core observation, and shallow geophysics (DiBiase et al., 2016) by the average hillslope lowering rates determined from ¹⁰Be concentrations in stream sediment. We assume no change in regolith storage on hillslopes, a colluvium density of 1500 kg m⁻³, a bedrock density of 2700 kg m⁻³, and we assume that the contributing area of sediment production is limited to the dip slopes that cover ~75% of the catchment area.

In order to evaluate potential fill histories consistent with cosmogenic data, we modeled the accumulation of cosmogenic ²⁶Al and ¹⁰Be in a 1-dimensional, 6.5 m-thick valley fill for comparison with buried samples from the Garner Run drill core. Specifically, we compared measured concentrations of ²⁶Al and ¹⁰Be ([²⁶Al] and [¹⁰Be]) with modeled concentrations from three scenarios: a single burial event, gradual burial, and pulsed burial. For each model scenario, we assume an inherited [²⁶Al] to [¹⁰Be] ratio of 6.5 and an inherited concentration of 4.0×10^5

atoms $\text{g}^{-1} \text{}^{10}\text{Be}$ (the average ratio and concentration of amalgamated boulder samples, respectively). We assume a surface production ratio of $[\text{}^{26}\text{Al}]$ to $[\text{}^{10}\text{Be}]$ of 6.5. For simplicity, we assign depths of 3.4, 4.8 and 6.4 to the clasts for the following calculations but acknowledge a range in depths for each clast as discussed above. For details on modeling schemes, see the Appendix C.

Because we have some constraint on possible inherited $[\text{}^{26}\text{Al}]/[\text{}^{10}\text{Be}]$, we could test whether the assumption of an inheritance ratio of 6.5 is reasonable. We ran a Monte Carlo simulation in which an inheritance ratio was chosen from a normal distribution of 1,000 values with a mean of 6.5.

RESULTS

Topographic Analysis

Lidar-derived topographic data indicate that gradients of Tuscarora Formation hillslopes mirror that of the underlying structure of plunging folds throughout central Pennsylvania. Within the Garner Run subcatchment, the south-facing planar hillslopes of Tussey Mountain maintain nearly constant gradient and orientation, whereas the north-facing slopes of Leading Ridge steepen with distance down-valley. Throughout Shavers Creek, subtle cuestas on the south-facing hillslope appear to show shadow bedding planes dipping slightly steeper than the slope gradient (Fig. 1a and b; Brantley et al., 2016).

In contrast to the dip slopes, the toeslope of the south-facing slope of Tussey Mountain contains a low-sloping bench marked at the surface by lobate structures oriented oblique to the valley axis (Fig. 2b). This bench widens down-valley, and in most places these lobes have pinned Garner Run to the north-facing slope of Leading Ridge; where these lobes are less prominent, the channel flows toward the center of the valley axis. In locations where Garner Run appears to

intersect and incise through surface lobes, the channel banks show exposure of colluvial fill up to 5 m thick.

From the lidar slopeshade map, we observe a number of small and large mass movements that we interpret to be slides and slumps in the upper few meters of regolith (Brantley et al., 2016, Fig. 6). These features are tens to hundreds of meters across, and appear as either angular or curvilinear scars with hummocky landslide deposits downslope. Topographic profiles drawn across these scars indicate that smaller slumps excavate and extrude ~2 m of regolith, while the debris from larger slides is 5-10 m thick.

Field Mapping of Regolith Texture

In general, much of the central Pennsylvania landscape underlain by the Tuscarora Formation is covered in boulders to varying degrees, with only occasional bedrock exposure along ridgelines (Fig. 2b). In the Garner Run subcatchment, field mapping results show the southeast-facing slope is generally more boulder-mantled, and that soil-mantled areas are largely confined to the low-sloping valley floor. Within the valley floor, lobes are flanked by boulders but are soil-mantled on top. Downstream of the study catchment, where lobate features are prominent, incision into the valley fill exposes coarse blocky debris overlain by fine-grained material which blankets the entire topographic bench. At and within 200 m of the ridgelines of both north- and south-facing slopes, large blocky debris fields form linear patterns that trend roughly parallel to the strike of the underlying bedrock.

Shallow soil pits showed that, on the south-facing dip slope of Tussey Mountain, a grey, eluviated E horizon occurred between the O/A horizons and the red, clay-rich B horizon and was up to 15 cm thick (see Appendix B). However, this soil horizon thins in sites downslope and completely disappears at sites in valley floor. The material mantling the low-sloping bench consists

of mainly soil or a boulder/soil mix and exhibits a clayey B horizon just below the surface. Shallow excavations (0.5-1.0 m) of rocky areas revealed that surficial rocks corresponded to rocks at depth and occurred within both E and B horizons.

Grain Size Analysis of Surface Clasts and Hillslopes and in Channels

On the hillslopes in the Garner Run subcatchment, we observed a general decrease in the intermediate axis length of boulders downslope of both Tussey Mountain and Leading Ridge (Fig. 3 and Table A2). While median clast size only varied by 10-20 cm from ridgeline to valley axis (average $D_{50} = 31$ to 22 cm), maximum block size dropped off significantly downslope (average $D_{max} = 88$ to 61 cm). The largest grains (> 1.0 m) were generally restricted to blockfields near ridgelines. Cobbles and boulders in canopied and open blockfields are generally larger than those embedded in a soil matrix, regardless of hillslope position. Mean D_{50} , D_{84} and D_{max} all decrease from open blockfields to canopied blockfields to boulder/soil mix. In a Student's t-test, the median grain size of all boulder/soil sites is different than canopied boulder fields and open boulder fields at confidence $p < 0.01$, and the D_{84} of the groups are different at $p < 0.005$. Clasts in open boulder fields bore sharp edges, while clasts in canopied boulder fields and those in a soil matrix tended to exhibit rounder edges. Most clasts were tabular, and short axes rarely exceeded 25 cm in length.

Within the Garner Run subcatchment, the median grain size of streambed sediment ($D_{50} = 15$ cm) tends to be finer than the lowermost hillslope clasts ($D_{50} = 25$ cm), but with similar shape and angularity (Fig. 4, 5). The channel site with the largest clasts ($D_{50} = 20$ cm) is directly adjacent to a boulder-lined lobe that feeds into the channel from Tussey Mountain. Down-valley and farther from adjacent ridgelines, channel sediment shows evidence of sorting, rounding, and downstream fining (Fig. 4). At the location 5 km downstream of the Garner Run headwaters, river cobbles are smaller and more rounded, and patches of underlying shale bedrock are exposed in the channel

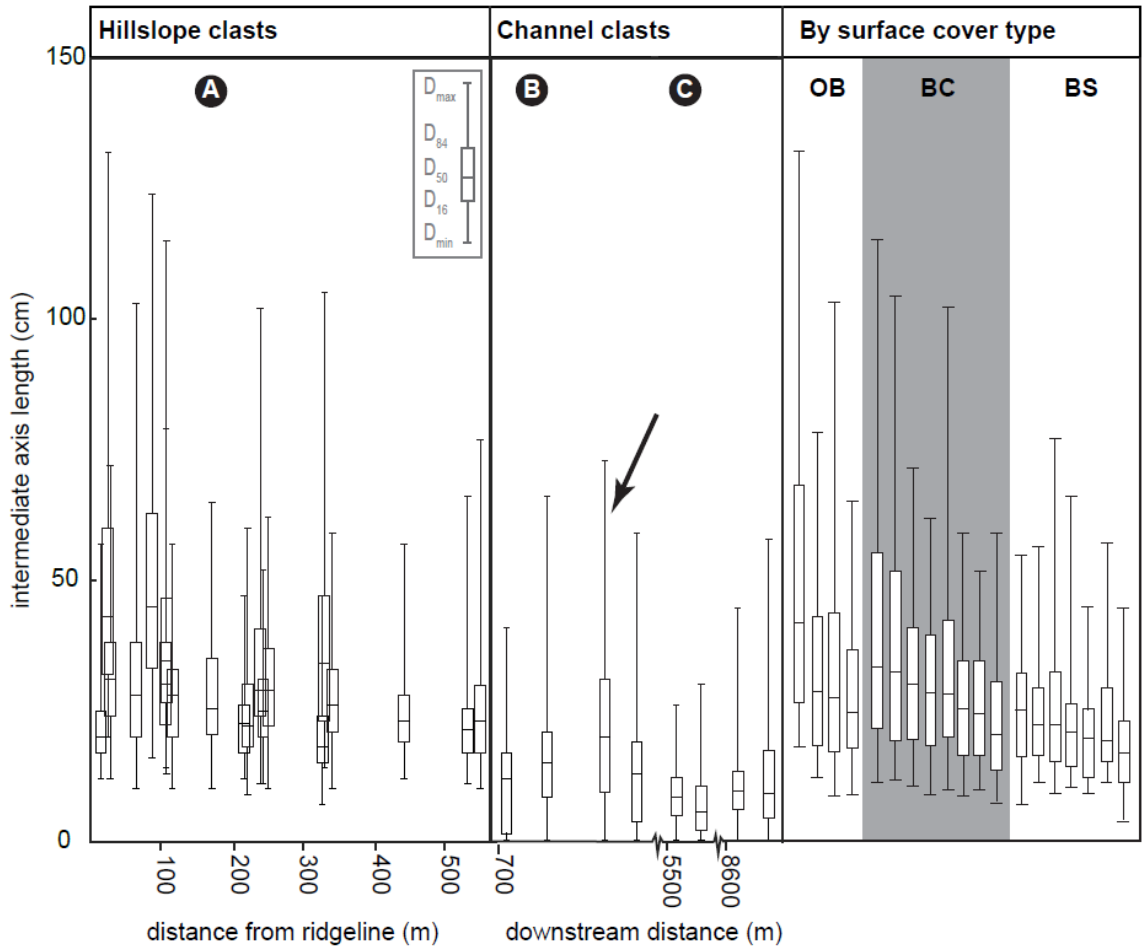


Fig. 3: Clast measurements from point counts conducted on hillslopes and in the channel. Generally, intermediate grain axes decrease with distance from the ridgelines, but most grains still measure >10 cm on the hillslopes whereas the channel contains smaller grains. However, the larger channel clasts are of similar size to hillslope boulders. Arrow points to site where solifluction lobe intersects stream, reflected as larger grain size at survey site. Circles “A,” “B” and “C” show locations of point-cloud models shown in Fig. 4.

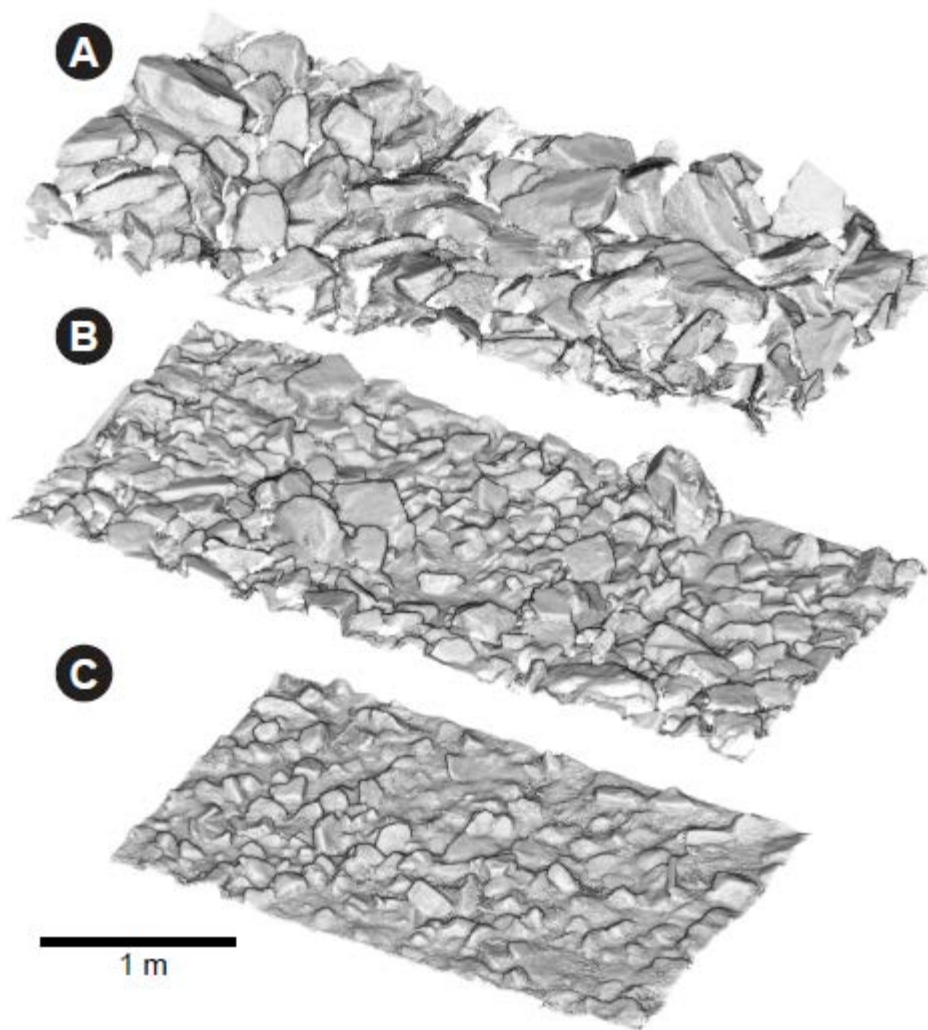


Fig. 4: Shaded-relief models of colluvium highlight clast size, shape and sorting differences between (A) open blockfield grains, (B) channel grains in the headwater and (C) channel grains ~5 km downstream of the subcatchment outlet.. Point clouds were generated through structure-from-motion photogrammetry and visualized in CloudCompare. These models demonstrate that in channels, most grains are smaller, rounded and better sorted than material in blockfields, and material is further fined and rounded downstream of headwaters.

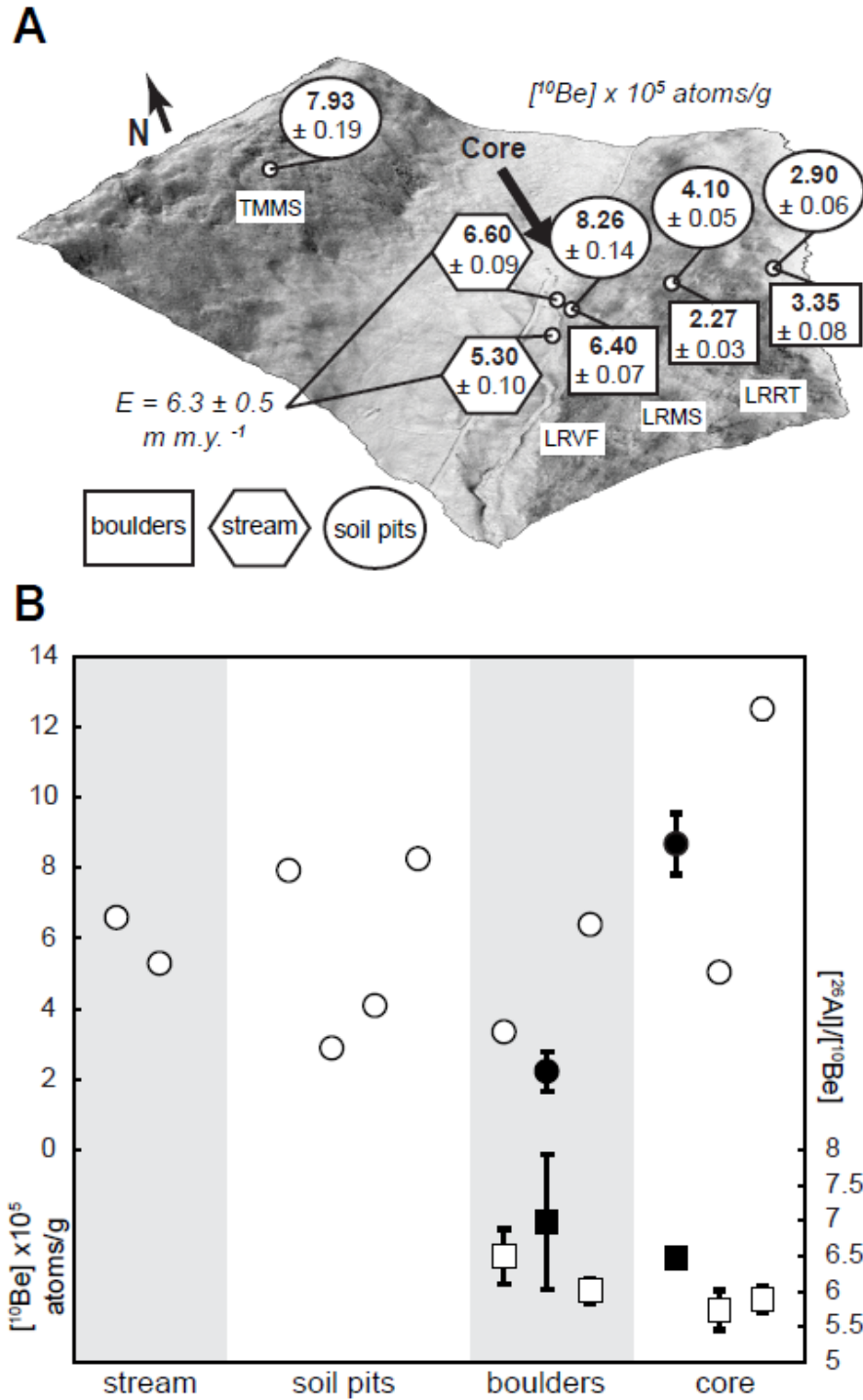


Fig. 5: (A) Summary of ^{10}Be concentrations in samples collected from soil pits (circles), surface boulders (rectangles) and stream sediments (hexagons) in the Garner Run subcatchment. The two stream sediment samples render an average erosion rate of $6.3 \text{ m} \pm 0.5 \text{ m m.y.}^{-1}$. (B) Plotted graphically, we demonstrate the overlap of measured ^{10}Be concentrations (circles) in surface samples. We also show ^{10}Be concentrations of core samples, which tend to be higher in

concentration than surface samples. We also show $[^{26}\text{Al}]/[^{10}\text{Be}]$ (squares) of boulder and core samples. Where one measurement was taken on a sample (white symbols) we show the point measurement and analytical uncertainty; where replicate measurements were taken on a single sample (black symbols), we show the mean and standard error.

floor. Where Garner Run steepens across the knickpoint at a Tuscarora anticline, coarse material again emerges in the channel coincident with steeper hillslopes, located adjacent to channel banks.

Cosmogenic Nuclide Analysis

Measured surface ^{10}Be concentrations at Garner Run range from $2 - 8 \times 10^5$ atoms g^{-1} , with similar average concentrations between soil samples, amalgamated boulder samples, and detrital sand samples (Table 1 and Fig. 5a and b). ^{10}Be concentrations in soil samples from the north-facing slope of Leading Ridge increase downslope, whereas ^{10}Be concentrations in surface boulders show no pattern. The single soil sample from the mid-slope of Tussey Mountain shows the highest ^{10}Be concentration measured in surface material. ^{10}Be concentrations in two stream sediment samples are similar to the average of all soil and amalgamated surface boulder samples, and indicate a catchment-average hillslope lowering rate of 6.3 ± 0.5 m m.y.^{-1} , assuming steady erosion over an integration timescale of ~ 100 kyr. Similarly, individual samples reflect 40 – 140 kyr of exposure. The ratio of $[^{26}\text{Al}]$ to $[^{10}\text{Be}]$ in the amalgamated surface boulder transects is 6.49 ± 0.49 .

If we assume the cored clasts were buried with a $[^{26}\text{Al}]$ to $[^{10}\text{Be}]$ ratio of 6.5, consistent with modern surface clasts, the bottom two clasts indicate significant burial whereas the top clast shows no burial signal (Fig. 6). The absolute concentrations of the three samples also indicate varying degrees of dosing on the hillslopes prior to burial: the upper two samples have ^{10}Be concentrations similar to amalgamated surface clasts (GR10 and GR11, 8.73 and 5.04×10^5 atoms g^{-1} , respectively), while the lowest sample (GR12) has a much higher concentration (12.5×10^5 atoms g^{-1} m^{-1}),) than any surface sample.

Constraining Colluvial Fill History

Given the surface area of the Garner Run hillslopes and fill debris, along with debris volume estimates, the valley fill is equivalent to $1.8 \text{ m} \pm 0.9 \text{ m}$ of bedrock erosion. This volume

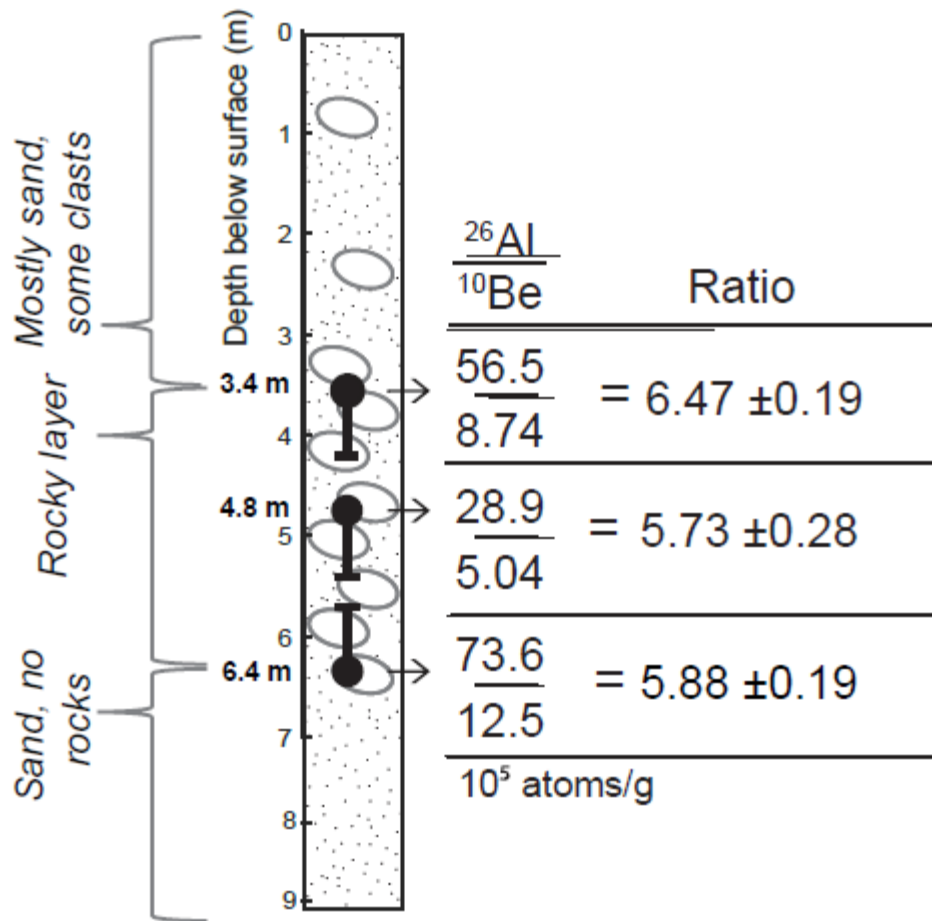


Fig. 6: Core samples taken from within the HV1 core at depths of 3.4 m, 4.8 m and 6.4 m below the surface. This interval between 3.4 and 6.4 m is a discrete rocky layer, overlying sand between 9.1 and 6.4 m depth and covered by a mix of sand and two clasts from unknown depths from 3.4 to 0 m below the surface. We show ^{26}Al and ^{10}Be concentrations, in 10^5 atoms per gram. We also calculate ratios between nuclides. Error bars indicate sample depth uncertainty up to 0.5 m.

TABLE 1. Cosmogenic nuclide data and calculated ratios

Sample location, type	Lab code	Easting	Northing	Elevation	[¹⁰ Be] (10 ⁵ atoms g ⁻¹)	[²⁶ Al] / [¹⁰ Be]
TMMS, soil	GR03	252907	4509540	575 m	7.93 ± 0.137	ND
LRRT, soil	GR04	253361	4508879	586 m	2.89 ± 0.0564	ND
LRMS, soil	GR05	253283	4508992	555 m	4.09 ± 0.0543	ND
LRVF, soil	GR06	253165	4509111	526 m	8.26 ± 0.137	ND
LRRT, rock	GR07	253361	4508879	586 m	3.35 ± 0.0817	6.49 ± 0.39
LRMS, rock*	GR08	253283	4508992	555 m	2.25 ± 0.0572	6.98 ± 0.94
LRVF, rock	GR09	253165	4509111	526 m	6.39 ± 0.0728	6.00 ± 0.17
Stream, upstream	GR01	253238	4508706	501 m	6.59 ± 0.0947	ND
Stream, downstream	GR02	253138	4509106	483 m	5.29 ± 0.0616	ND
Core, top*	GR10	253370	4509326	3.4 m**	8.67 ± 0.0873	6.47 ± 0.00
Core, middle	GR11	253370	4509326	4.8 m**	5.04 ± 0.0961	5.73 ± 0.28
Core, bottom	GR12	253370	4509326	6.4 m**	12.5 ± 0.271	5.88 ± 0.19

*Values are means and standard error of the mean calculated from one original and one replicate sample
**Depths below drilling surface at elevation 0 m.

represents 300 ± 150 kyr of steady bedrock lowering, given our estimated long-term erosion rate of 6 m m.y.^{-1} .

For the single-burial scenario (Fig. 7a), we assumed that all core material was deposited at once, and we tracked the production and decay of ^{26}Al and ^{10}Be for a range of burial ages between 15-400 ka. As noted above, the lower two clasts require significant burial ($250 \text{ ka} \pm 100 \text{ ka}$ for the bottom sample and $270 \text{ ka} \pm 100 \text{ ka}$ for the middle sample) than the uppermost clast ($< 15 \text{ ka}$). Although the $[\text{}^{26}\text{Al}]/[\text{}^{10}\text{Be}]$ is close enough to the modeled inheritance ratio, we chose 15 ka as a burial age for the latest Pleistocene. No single burial age is consistent with the $[\text{}^{26}\text{Al}]/[\text{}^{10}\text{Be}]$ measurements from all three samples.

For the steady accumulation rate scenario (Fig. 7b), we modeled the concentration of ^{26}Al and ^{10}Be in a steadily accumulating sediment package, and varied the date at which sediment began to accumulate from 15-400 ka, corresponding to deposition rates of 13 to 1.6 m k.y.^{-1} . Similar to the single-burial scenario, there is no constant accumulation rate that explains the $^{26}\text{Al}/^{10}\text{Be}$ ratio of the three samples.

For the pulsed burial scenario (Fig. 7c), we modeled a two-stage burial history consisting of deposition of the lower 3.0 m of fill (spanning the two lower samples and fill between the middle and upper sample, at final depths of 6.5 to 3.5 m) in a single event, followed by a hiatus and then deposition of the upper 3.4 m in a single event, including the upper clast. We set the depth of the hiatus surface to 3.7 m based on constraints from the middle clasts' concentration of ^{10}Be (see Data Repository). Here we find a burial age of $290 \text{ ka} \pm 50 \text{ ka}$ for the first pulse fit our observed data well. We assign a burial age of 15 ka to the upper clast based on the date of warming associated with the end of the LGM (Watts, 1979).

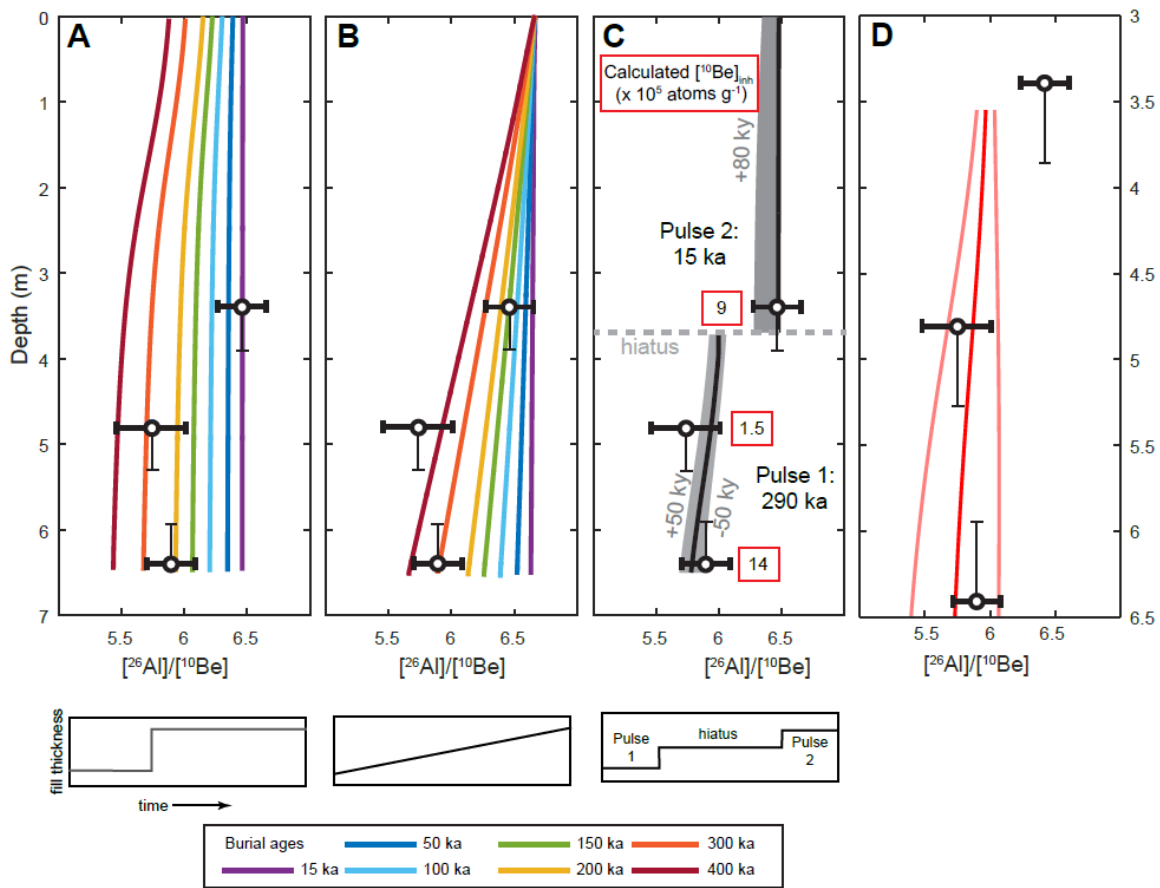


Fig. 7: Forward-model outputs simulating deposition of debris recovered from valley core, along with schematic diagrams of the depositional scenario. (A) Modeled $^{26}\text{Al}/^{10}\text{Be}$ ratios of core material with depth given a single deposition event. Contours are labeled by timing of deposition, in kyr before present. The schematic diagram below shows accumulation of all cored material at a single time. (B) Modeled $^{26}\text{Al}/^{10}\text{Be}$ ratios of core material given steady accumulation of core material. Contours are labeled by depositional rate, in cm per kyr. Faster accumulation rates are equivalent to more recent onset of accumulation, while slower accumulation rates are equivalent to accumulation beginning earlier, and all scenarios result in 6.4 m of accumulated debris. (C) Best-fitting $^{26}\text{Al}/^{10}\text{Be}$ given a pulsed model of accumulation, where bottom two clasts are deposited along with overlying fill in a single event, followed by deposition of the top sample along with overlying fill. Model outputs best match measured values when the first pulse accumulates 290 ka and the second pulse accumulates 15 ka. Gray shaded area shows range of burial age given analytic uncertainty. (D) Results from Monte Carlo simulation showing mean (solid red) and 1-sigma spread (light red) of simulations sampling for inheritance ratio.

While variable [^{10}Be] inheritance between the three clasts is necessary to explain the [^{10}Be] pattern with depth, varying the clasts' inheritance does not alter the modeled [^{26}Al]/[^{10}Be] enough to impact our interpretations. Likewise, the surface production ratio may be higher than our modern surface clast measurements' ratios, perhaps as high as 7.3 (Corbett et al., 2017a); a production ratio higher than our modeled 6.5 would mean our modeled results are minimum burial ages for the deposit.

Our Monte Carlo simulations, using variable inheritance ratios of [^{26}Al] to [^{10}Be] demonstrate that the suite of means for each modeled clast ratio falls within our analytic uncertainty.

DISCUSSION

Our field and topographic analyses suggest that periglaciation at Garner Run exerts a primary control on the spatial patterns in regolith texture and critical zone architecture. First, we synthesize field mapping and landscape morphology to show cold-climate processes are the principal mechanism for sediment production and downslope transport, with limited landscape modification by temperate processes. Then, we use both surface and buried cosmogenic nuclide samples to demonstrate regolith at Garner Run integrates the effects of multiple glacial cycles.

Controls on Spatial Variability in Regolith Texture and Morphology

We interpret the pattern of decreasing rockiness with distance downslope to be a signature of preferential transport of fine-grained material by permafrost thaw, which also drives the movement of the upper layers of soil in a process known as solifluction (Matsuoka, 2001) (Fig. 8). Solifluction lobes terminate at and fill the valley floor with clayey colluvium, consistent with the high water content of mass movement associated with thawing permafrost which preferentially transports finer particles within moving soil (French, 2013) as well as the subsurface eluviation of

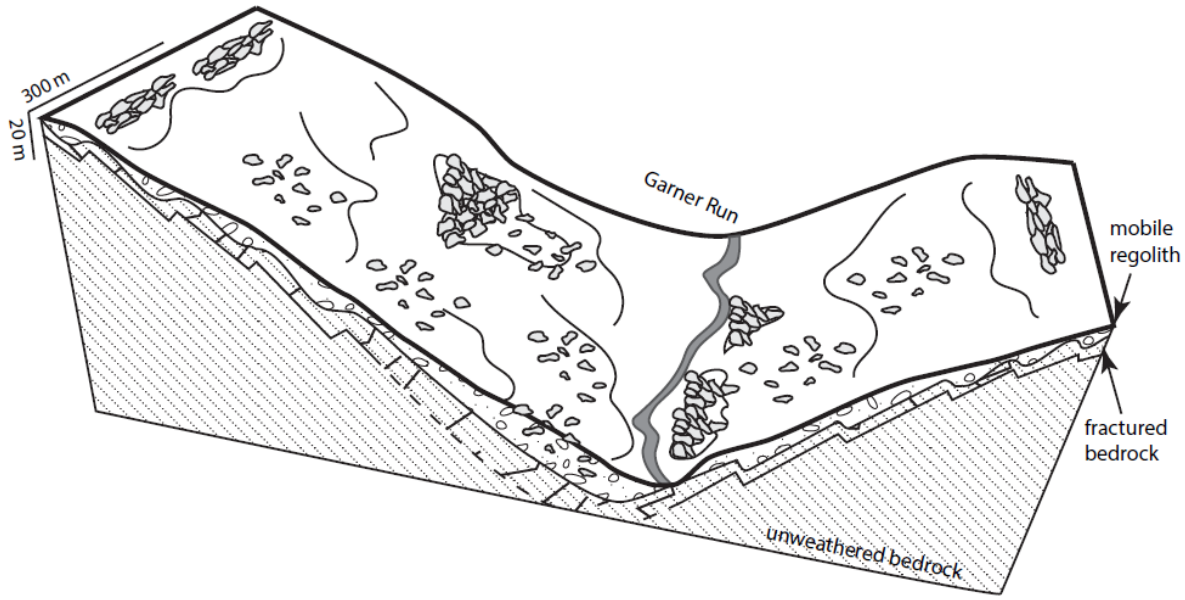


Fig. 8: Schematic diagram of geomorphology at the surface and subsurface at Garner Run. Both ridgeline and toeslope boulder fields represent areas where overlying regolith was removed during permafrost melt, exposing fractured bedrock (boulders not drawn to scale). These sites correspond to zones of shallower fractured bedrock as seen in ground-penetrating radar (DiBiase et al. 2016) and shown here as zones of fractured bedrock between mobile regolith and unweathered bedrock, which also appear as contrasting features in shallow geophysical imagery. Solifluction lobes mobilize fine-grained sediment from upslope and transport regolith, along with smaller boulders, into the valley floor. This valley fill accumulates as a thick wedge 5 m thick at the base of the south-facing Tussey Mountain. Garner Run is subsequently pushed toward the toeslope of the north-facing Leading Ridge hillslope, which instigates small slope failures near the banks. The stream incises through 1-5 m of solifluction fill before becoming entirely armored by blocky debris, at which point incision slows or stops until the next solifluction event. Thus, fill from multiple periglacial periods is deposited via solifluction and is preserved for hundreds of thousands of years in the valley floor.

clays within solifluction lobes (Carter and Ciolkosz, 1986), which we observe at Garner Run as thinning E horizons downslope. Transported particulate iron also accumulates in weathering rinds on boulders downslope (Gentoso, 2008). We interpret deeper failures that retain a discrete headscarp to be indicative of active-layer detachment slides along dip slopes (Lewkowitz and Harris, 2005a; Lewkowitz and Harris, 2005b).

Solifluction, as the primary agent for filing the valley axis with finer debris, also facilitates the movement of coarse blocky cobbles onto the toeslope and valley floor. Channel armoring via blocky debris, along with the magnitude of solifluction-derived sediment flux, limits fluvial incision into, and removal of, valley-bottom debris. From field and burial modeling observations, we infer that the thick wedge of periglacial hillslope debris at the foot of Tussey Mountain is the product of pulsed accumulation via solifluction over multiple glaciations. This influx of debris carried hillslope-derived blocks which have slowed or prevented subsequent fluvial incision into the fill (see Fig. 4); where the stream is clearly incising through the lobe debris, bed material is large, angular and, we assume, relatively immobile. We hypothesize that in the headwaters, channelized flow only incises through the periglacial debris as long as it can mobilize finer particles, such as the sand and clay we observed in both soil pits and drilling. Once those fines are selectively removed, the riverbed becomes armored by quartzite blocks that can only weather in-place, and incision slows dramatically or ceases. Such a boulder lag is observed in cut-banks 1 km downstream of the watershed top, where a package of boulders lacking interstitial fines is buried by a sandy-clayey solifluction lobe mantling the entire low-sloping bench. 5 km downstream, river cobbles are smaller and more rounded, and patches of underlying shale bedrock are exposed in the channel floor, indicating enhanced fluvial alteration of the channel and river cobbles.

We find that the pulsed deposition of fine-grained matrix and cobbles inferred from core stratigraphy and forward modeling is consistent with accumulation via solifluction during periglacial climate conditions. The depositional hiatus between 4.8 and 3.4 m depth, inferred from forward modeling, is consistent with winnowing of fines via streamflow and minimal valley-bottom sedimentation during an interglacial period, which would produce the boulder lag described above and observed within the dated core material. In contrast, the remaining 3.4 m of fill, deposited more recently, contains a mix of matrix and larger clasts, consistent with unaltered solifluction debris. Fine-grained material, either from the weathering of overlying units or from dust, would have been present on the hillslopes at the first pulse 290 ka in order to facilitate solifluction to produce valley fill. Thus, at Garner Run, we infer that valley sedimentation occurs in pulses during periglacial conditions, and this debris is reworked during interglacials, only to be covered again by solifluction delivered material during the next cold period.

We interpret the blockfields to be a lag of coarse material left behind after loss of fines, consistent with the observation that pervasive blockfields on Tussey Mountain correspond to more extensive colluvial deposits downslope. Mapped blockfields on both north- and south-facing slopes occur in linear patterns oriented parallel to underlying bedrock strike (see Fig. 3), evidence that the coarse lag is close to the bedrock interface. By removing upper layers of regolith, solifluction stripped finer-grained regolith material and exposed intact bedrock on dip slopes, preserved as blockfields. Shallow depths to bedrock are also inferred on hillslopes by the presence of subtle cuestas. Where boulders are mixed with interstitial soil, clasts tend to be smaller than those in blockfields, suggesting accelerated weathering in these areas. Compared to open blockfields, sites with soil would be well-suited to trap dust and hold moisture, thus facilitating more soil formation in interglacials. Our amalgamated boulder samples for cosmogenics, sampled

from boulder/soil mix areas, exhibit similarity in concentrations between boulder and sand fractions, implying similar downslope sediment exposure histories and thus virtual downslope velocities.

The prevalence of open blockfields and prominent solifluction lobes derived from Tussey Mountain, which appear to divert the channel toward the toeslope of Leading Ridge, suggest a higher sediment flux from the south-facing slopes than north facing slopes. Textural analyses on the soil pits at the SSHCZO show variable clay and rock fragment content with depth on north-facing slopes, but relatively constant clay and rock fragment content on the south-facing soil pit (Brantley et al., 2016). We attribute that pattern to the dominance of solifluction activity on the south-facing slope, as homogenized upper soil horizons in nearby soil catenas have been attributed to cryoturbation and permafrost thaw (Cronce, 1988). Although the south-facing slope is rockier and contains more open blockfields, the north-facing slope becomes rockier down-valley as the hillslope steepens with changing fold geometry. Thus, it is unclear the degree to which the observed contrast in boulder cover is due to aspect controls or is a consequence of structurally controlled slopes, which are steeper on the south-facing slope.

Colluvial Fill History and Implications for Hillslope-Channel Coupling

The fill represents 300 ± 150 kyr of steady bedrock lowering, given our measured long-term erosion rate of 6 m m.y.^{-1} and debris volume equivalent to $1.8 \text{ m} \pm 0.9 \text{ m}$ of bedrock erosion, which corresponds well to the minimum burial $[^{26}\text{Al}]/[^{10}\text{Be}]$ age of 290 ± 50 ka of the lower core material. As a minimum burial age for the entire package, the upper bound on the value of the lowest clast's ratio, $6.08 \times 10^5 \text{ atoms g}^{-1}$, requires a burial age of 150 ka.

The simple case that explains the data well – a pulse 290 ka and a pulse 15 ka – is consistent with geomorphic observations of pulsed deposition of periglacial debris, consisting of clasts within

a fine-grained matrix, followed by subsequent landscape steadiness. The lowest two clasts have similar $^{26}\text{Al}/^{10}\text{Be}$ ratios, consistent with the interpretation that the lower half of the fill reflects a pulse of burial consistent with glacial terminations at the end of marine isotope stages 8 or 10 at ~300 and ~250 ka, respectively (Lang and Wolff, 2011). The upper 3.4 m of fill, including the top clast sampled, is more consistent with burial within the most recent Wisconsinan glaciation (<50 ka). Both these arguments suggest that the colluvial fill records at least three glacial/interglacial cycles, implying that hillslope-derived periglacial debris is not entirely cleared from headwater valleys during interglacial periods. Instead, the debris persists long enough to be buried in a subsequent periglacial period. Without samples in between the middle and upper clasts, we can only speculate whether glacial/interglacial transitions between 290 ka and LGM would have deposited material; given the 100-kyr glacial cycles at the end of the Pleistocene, denser sampling in that interval would clarify whether every transitional period encodes a sedimentological record.

The analytical uncertainties in ^{26}Al measurements means that individual ratio-derived burial ages can be known to a precision of $\pm \sim 80$ kyr; here, we constrain the age of the first pulse by taking into account the analytical uncertainty of two samples thus reducing possible burial date to a range of ± 50 kyr. Though we model burial of the upper half to be of LGM age (15 ka), given analytical uncertainty the second pulse could be dated as early as 80 ka.

While our model interpretation of burial timing with nuclide ratios is not dependent on knowing each clast's inheritance, the three clasts need variable inheritance to best fit the observed absolute concentrations of ^{26}Al and ^{10}Be . Specifically, in order for the bottom two clasts to exhibit roughly the same burial history but very different total concentrations of nuclides (5.04 versus 12.5×10^5 atoms g^{-1} ^{10}Be), the bottom clast would have needed considerable hillslope exposure prior to burial while the middle clast would have had very little exposure. While these data may reflect and

change in hillslope sediment production, individual clasts may experience more or less hillslope exposure depending on localized hillslope processes.

Our catchment erosion rate of 6 m m.y.^{-1} and fill age suggests periglaciation does not represent many meters' worth of bedrock removed in a single climate transition, as had been previously hypothesized in central Appalachia (Braun, 1989). Instead, the minimum age of the fill, as well as the preservation of periglacial landscape features, imply periglacial debris is the composite result of many climate cycles, which has been found of other relict periglacial environments (Wilson et al., 2008; Denn et al., 2017). The age of the fill derived from cosmogenics ($290 \text{ ka} \pm 50 \text{ ka}$) is well-predicted by integrating the accumulation of debris via steady erosion of the hillslopes ($300 \pm 150 \text{ kyr}$), implying that, in the long term, rapid yet short-lived periglacial erosion during, or in transitions to and from, glacial periods is balanced by slow erosion in temperate climates. One caveat to our interpretations is that this landscape may violate the assumption that hillslopes are denuded steadily, and the subsequent debris is well-mixed (Granger and Riebe, 2014). The pulsed nature of sediment transport in this landscape, while important on short timescales, becomes indistinguishable from steady processes on the long ($38\text{-}140 \text{ kyr}$) timescales over which our cosmogenic samples integrate.

Garner Run's location upstream of a knickpoint may also hinder the evacuation of colluvial valley fill. A subcatchment insulated from regional base level fall can locally preserve hillslope-derived sediment as valley fill. Downstream of the knickpoint below Garner Run, erosion rates at the Shale Hills subcatchment are two to three times higher than those measured at Garner Run, and regolith post-dates the LGM (West et al., 2013). However, previous workers speculated that in sandstone headwater catchments, immobile periglacial sediment controls river slope in headwater basins (Hack, 1957; Brush Jr., 1961; Pizzuto, 1995), further slowing the propagation of

any base level fall. We show here that this combination of knickpoint location and immobile debris has prevented significant river incision in the headwater for hundreds of thousands of years and preserving the low-gradient channel. Our interpretations are important for analyzing the history of landscape steadiness recorded in Valley and Ridge river basins, including whether spatial variations in channel incision are controlled by base level, lithology or climate.

Implications for the Evolution of the Critical Zone

The lithologic and structural control on periglacial debris storage, demonstrated here at Garner Run, implies structural traps common within the Valley and Ridge's tightly folded sandstone units can facilitate thick sediment accumulation in headwater catchments. This sedimentary record of climate change presents a unique opportunity to study climate-modulated erosion across many climate cycles. Both the timescale of sediment storage and direct transfer of hillslope debris to burial in valleys make sedimentary records in central Appalachian headwater valleys unique archives for erosion rates and mechanisms. Individual sandstone units like the Tuscarora span north-south throughout the unglaciated Appalachians and thus paleoclimate gradients for further exploration of climate control on erosional efficiency. Moreover, the addition of paleoecological records such as pollen assemblages can create multi-proxy records of both timing and paleoclimate conditions of buried sedimentary records, which have the ability to directly link climate changes to changes in erosion rates (e.g. Litwin et al., 2013; Miller et al., 2014).

The persistence of regolith at Garner Run means that critical zone at this site integrates over multiple climate cycles, which set boundary conditions like moisture, temperature and biota, which control the pace and pattern of critical zone processes (Anderson et al., 2007; Brantley and Lebedeva, 2011). Previous work on Valley and Ridge periglacial features, drawing on ^{14}C and

thermoluminescence ages, date fine-grained periglacial slope material (Clark and Ciolkosz, 1988), and work at the nearby Shale Hills catchment shows regolith post-dates the LGM (West et al., 2013). However, boulders themselves have older and complex exposure history and thus landforms may be composite features with complex erosional histories (e.g. Wilson et al., 2008; Denn et al., 2017). Likewise soil properties with depth are not just a function of modern pedogenesis but also ancient sediment transport and cold-weather processes (Ciolkosz et al., 1990). Heterogeneity in the regolith and shallow subsurface, shaped by relict climate conditions, controls modern hydrology by modulating infiltration and subsurface flow paths and are thus important considerations for hydrologic models (McDonnell et al., 2007; Shi et al., 2013) as well as interpreting modern fluxes of mass and energy in the critical zone (Brantley and Lebedeva, 2011).

CONCLUSIONS

In this study, we analyzed field and remotely-sensed data from a sandstone headwater valley to document mechanisms of periglacial landscape alteration, and we paired these observations to cosmogenically-derived exposure ages, burial ages, and erosion rates. Core stratigraphy and burial dating indicate periods of pulsed accumulation as well as depositional hiatuses that produce textural variation in the core that match observations at the surface. We argue that the dominant erosional mechanisms in this headwater catchment occur in periglacial conditions, facilitating the freezing and rapid thaw of the top layers of regolith. Buried debris in the valley, the products of periglacial erosion, integrate over multiple climate cycles in the Pleistocene. Periglacial mechanisms appear to be the dominant geomorphic agent in these headwater catchments; the relatively vigorous sediment transport in these cold times is balanced

by relative landscape stability during warmer climate conditions Our measured catchment erosion rate (6 m m.y.^{-1}) as an integration of glacial and interglacial erosion rates.

Periglacial landscape modification affected both hillslope relief structure and bedload/channel profiles, as well as the modern critical zone, affecting present-day water, solute and sediment fluxes. Results show potential for periglacial headwater catchments in central Appalachia to preserve a direct record of cold-climate hillslope processes. The short source-to-sink path of sediment stored in central Appalachian headwater valleys increased the potential to preserve both cosmogenic dating and paleoclimate records on a latitude gradient.

References

- Anderson, R.S., Anderson, S.P., and Tucker, G.E., 2013, Rock damage and regolith transport by frost: an example of climate modulation of the geomorphology of the critical zone: *Earth Surface Processes and Landforms*, v. 38, no. 3, p. 299–316, doi: 10.1002/esp.3330.
- Anderson, S.P., von Blanckenburg, F., and White, A.F., 2007, Physical and chemical controls on the critical zone: *Elements*, v. 3, no. 5, p. 315–319, doi: 10.2113/gselements.3.5.315.
- Brantley, S.L., Dibiase, R., Russo, T., Shi, Y., Lin, H., Davis, K.J., and Kaye, M., 2016, Designing a suite of measurements to understand the critical zone: *Earth Surface Dynamics*,.
- Brantley, S.L., and Lebedeva, M., 2011, Learning to Read the Chemistry of Regolith to Understand the Critical Zone: *Annual Review of Earth and Planetary Sciences*, v. 39, no. 1, p. 387–416, doi: 10.1146/annurev-earth-040809-152321.
- Braun, D.D., 1989, Glacial and periglacial erosion of the Appalachians: *Geomorphology*, v. 2, no. 1–3, p. 233–256, doi: 10.1016/0169-555X(89)90014-7.
- Brush Jr., L.M., 1961, Drainage basins, channels, and flow characteristics of selected streams in central Pennsylvania: U.S. Geological Survey Professional Paper 282-F, p. 145–181.
- Carter, B.J., and Ciolkosz, E.J., 1986, Sorting and thickness of waste mantle material on a sandstone spur in central Pennsylvania: *Catena*, v. 13, no. 6973, p. 241–256.
- Ciolkosz, E.J., Carter, B.J., Hoover, M.T., Cronce, R.C., Waltman, W.J., and Dobos, R.R., 1990, Genesis of soils and landscapes in the Ridge and Valley province of central Pennsylvania: *Geomorphology*, v. 3, no. 3–4, p. 245–261, doi: 10.1016/0169-555X(90)90006-C.
- Ciolkosz, E., Drohan, P., and Sevon, W., 2008, The Pleistocene record In the middle and lower Susquehanna River Basin and the longer term evolution of the Susquehanna Basin landscape, *in* 20th Biennial Meeting of the American Quaternary Association, University Park, p. 1–58.
- Clark, G.M., Behling, R.E., Braun, D.D., Ciolkosz, E.J., Kite, J.S., and Marsh, B., 1992, Central Appalachian Periglacial Geomorphology, *in* Agronomy Series Number 120,.
- Clark, G.M., and Ciolkosz, E.J., 1988, Periglacial geomorphology of the Appalachian highlands and interior highlands south of the glacial border — A review: *Geomorphology*, v. 1, no. 3, p. 191–220, doi: 10.1016/0169-555X(88)90014-1.
- Corbett, L.B., Bierman, P.R., Rood, D.H., Caffee, M.W., Lifton, N.A., and Woodruff, T.E.,

- 2017a, Cosmogenic $^{26}\text{Al}/^{10}\text{Be}$ Surface Production Ratio in Greenland: Geophysical Research Letters, p. 1350–1359, doi: 10.1002/2016GL071276.
- Corbett, L.B., Bierman, P.R., Stone, B.D., Caffee, M.W., and Larsen, P.L., 2017b, Cosmogenic nuclide age estimate for Laurentide Ice Sheet recession from the terminal moraine, New Jersey, USA, and constraints on latest Pleistocene ice sheet history: Quaternary Research, p. 1–17, doi: 10.1017/qua.2017.11.
- Cronce, R.C., 1988, The genesis of soils overlying dolomite in the Nittany Valley of central Pennsylvania: Pennsylvania State University, 388 p.
- DiBiase, R., Del Vecchio, J., Mount, G., Hayes, J.L., Comas, X., Guo, L., Lin, H., Zarif, F., Forsythe, B., and Brantley, S.L., 2016, Quantifying the spatial variability in critical zone architecture through surface mapping and near-surface geophysics, in 2016 Fall Meeting, American Geophysical Union, San Francisco, CA.
- Flueckinger, L.A., 1969, Report 176, Geology of a Portion of the Allensville Quadrangle, Centre and Huntingdon Counties, Pennsylvania.:
- French, H.M., 2013, The periglacial environment: Third edition:
- Gentoso, M., 2008, Boulder Fields of the Tuscarora Formation: The Pennsylvania State University College of Earth and Mineral Sciences.
- Granger, D.E., 2006, A review of burial dating methods using ^{26}Al and ^{10}Be : Geological Society of America Special Papers, v. 415, no. 1, p. 1–16, doi: 10.1130/2006.2415(01).
- Granger, D.E., and Riebe, C.S., 2014, Cosmogenic Nuclides in Weathering and Erosion: Elsevier Ltd.
- Hack, J.T., 1957, Studies of longitudinal stream profiles in Virginia and Maryland: USGS Professional Paper 249, p. 97.
- Hallet, B., Hunter, L., and Bogen, J., 1996, Rates of erosion and sediment evacuation by glaciers: A review of field data and their implications: Global and Planetary Change, v. 12, no. 1–4, p. 213–235, doi: 10.1016/0921-8181(95)00021-6.
- Kneller, M., and Peteet, D., 1999, Late-Glacial to Early Holocene Climate Changes from a Central Appalachian Pollen and Macrofossil Record: Quaternary Research, v. 147, p. 133–147, doi: 10.1006/qres.1998.2026.
- Koppes, M.N., and Montgomery, D.R., 2009, The relative efficacy of fluvial and glacial erosion over modern to orogenic timescales: Nature Geoscience, v. 2, no. 9, p. 644–647, doi:

10.1038/ngeo616.

- Kovar, A.J., 1965, Pollen analysis of the Bear Meadows Bog of Central Pennsylvania: Proceedings of the Pennsylvania Academy of Science, v. 38, no. June.
- Lang, N., and Wolff, E.W., 2011, Interglacial and glacial variability from the last 800 ka in marine, ice and terrestrial archives: *Climate of the Past*, v. 7, no. 2, p. 361–380, doi: 10.5194/cp-7-361-2011.
- Lewkowicz, A.G., and Harris, C., 2005a, Frequency and Magnitude of Active-layer Detachment Failures in Discontinuous and Continuous Permafrost , Northern Canada: *Permafrost and Periglacial Processes*, v. 130, no. April 2004, p. 115–130, doi: 10.1002/ppp.522.
- Lewkowicz, A.G., and Harris, C., 2005b, Morphology and geotechnique of active-layer detachment failures in discontinuous and continuous permafrost, northern Canada: *Geomorphology*, v. 69, no. 1–4, p. 275–297, doi: 10.1016/j.geomorph.2005.01.011.
- Litwin, R.J., Smoot, J.P., Pavich, M.J., Markewich, H.W., Brook, G., and Durika, N.J., 2013, 100,000-year-long terrestrial record of millennial-scale linkage between eastern North American mid-latitude paleovegetation shifts and Greenland ice-core oxygen isotope trends: *Quaternary Research (United States)*, v. 80, no. 2, p. 291–315, doi: 10.1016/j.yqres.2013.05.003.
- McDonnell, J.J., Sivapalan, M., Vach??, K., Dunn, S., Grant, G., Haggerty, R., Hinz, C., Hooper, R., Kirchner, J., Roderick, M.L., Selker, J., and Weiler, M., 2007, Moving beyond heterogeneity and process complexity: A new vision for watershed hydrology: *Water Resources Research*, v. 43, no. 7, p. 1–6, doi: 10.1029/2006WR005467.
- Miller, I.M., Pigati, J.S., Scott Anderson, R., Johnson, K.R., Mahan, S.A., Ager, T.A., Baker, R.G., Blaauw, M., Bright, J., Brown, P.M., Bryant, B., Calamari, Z.T., Carrara, P.E., Cherney, M.D., et al., 2014, Summary of the Snowmastodon Project Special Volume. A high-elevation, multi-proxy biotic and environmental record of MIS 6-4 from the Ziegler Reservoir fossil site, Snowmass Village, Colorado, USA: *Quaternary Research*, v. 82, no. 3, p. 618–634, doi: 10.1016/j.yqres.2014.07.004.
- OpenTopography, 2010, Susquehanna Shale Hills Critical Zone Observatory: Leaf Off Survey: , doi: 10.5069/G9VM496T.
- PAMAP Program, 2006,.
- Pizzuto, J.E., 1995, Downstream fining in a network of gravel-bedded rivers: *Water Resources*

- Research, v. 31, no. 3, p. 753–759, doi: 10.1029/94WR02532.
- Portenga, E.W., Bierman, P.R., Trodick, C.D., Greene, S.E., DeJong, B.D., Rood, D.H., and Pavich, M.J., 2017, Background rates of erosion and sediment generation in the Potomac River basin, USA, derived using in situ ^{10}Be , meteoric ^{10}Be , and ^9Be : *Geological Society of America Bulletin*, , no. Xx, p. B31543.1, doi: 10.1130/B31543.1.
- Ramage, J.M., Gardner, T.W., and Sasowsky, I.D., 1998, Early Pleistocene Glacial Lake Lesley , West Branch Susquehanna River valley , central Pennsylvania: *Geomorphology*, v. 22, p. 19–37.
- Reusser, L.J., Bierman, P.R., Pavich, M.J., and Zen, E., 2004, Rapid Late Pleistocene Incision of Atlantic Passive-Margin River Gorges: *Science*, v. 305, p. 499–502, doi: 10.1126/science.1097780.
- Shi, Y., Davis, K.J., Zhang, F., and Duffy, C.J., 2013, Development of a Coupled Land Surface Hydrologic Model and Evaluation at a Critical Zone Observatory: *Journal of Hydrometeorology*, v. 14, p. 1409–1419, doi: 10.1175/JHM-D-12-0145.1.
- Shuman, B., 2002, The Anatomy of a Climate Oscillation: Vegetation Change in Eastern North America During the Younger Dryas Chronozone: *Quaternary Science Reviews*, v. 21, p. 1777–1792.
- Shuman, B.N., and Marsicek, J., 2016, The structure of Holocene climate change in mid-latitude North America: *Quaternary Science Reviews*, v. 141, p. 38–51, doi: 10.1016/j.quascirev.2016.03.009.
- Thomas, E.M., Lin, H., Duffy, C.J., Sullivan, P.L., Holmes, G.H., Brantley, S.L., and Jin, L., 2013, Spatiotemporal Patterns of Water Stable Isotope Compositions at the Shale Hills Critical Zone Observatory: Linkages to Subsurface Hydrologic Processes: *Vadose Zone Journal*, v. 12, no. 4, p. 0, doi: 10.2136/vzj2013.01.0029.
- Vandenberghe, J., French, H.M., Gorbunov, A., Marchenko, S., Velichko, A.A., Jin, H., Cui, Z., Zhang, T., and Wan, X., 2014, The Last Permafrost Maximum (LPM) map of the Northern Hemisphere: Permafrost extent and mean annual air temperatures, 25-17ka BP: *Boreas*, v. 43, no. 3, p. 652–666, doi: 10.1111/bor.12070.
- Watts, W.A., 1979, Late Quaternary vegetation of central Appalachia and the New Jersey coastal plain.: *Ecological Monographs*, v. 49, no. 4, p. 427–469, doi: 10.2307/1942471.
- West, N., Kirby, E., Bierman, P., Slingerland, R., Ma, L., Rood, D., and Brantley, S., 2013,

- Regolith production and transport at the Susquehanna Shale Hills Critical Zone Observatory, part 2: Insights from meteoric ^{10}Be : *Journal of Geophysical Research: Earth Surface*, v. 118, no. 3, p. 1877–1896, doi: 10.1002/jgrf.20121.
- Westoby, M.J., Brasington, J., Glasser, N.F., Hambrey, M.J., and Reynolds, J.M., 2012, “Structure-from-Motion” photogrammetry: A low-cost, effective tool for geoscience applications: *Geomorphology*, v. 179, p. 300–314, doi: 10.1016/j.geomorph.2012.08.021.
- Whipple, K.X., and Tucker, G.E., 1999, Dynamics of the stream-power river incision model: Implications for height limits of mountain ranges, landscape response timescales, and research needs: *Journal of Geophysical Research*, v. 104, no. B8, p. 661–674.
- Williams, J.W., Shuman, B.N., Webb, T., Bartlein, P.J., and Leduc, P.L., 2004, Late-Quaternary vegetation dynamics in North America: Scaling from taxa to biomes: *Ecological Monographs*, v. 74, no. 2, p. 309–334, doi: 10.1890/02-4045.
- Wilson, P., Bentley, M.J., Schnabel, C., Clark, R., and Xu, S., 2008, Stone run (block stream) formation in the Falkland Islands over several cold stages, deduced from cosmogenic isotope (^{10}Be and ^{26}Al) surface exposure dating: *Journal of Quaternary Science*, v. 23, no. 5, p. 461–473, doi: 10.1002/jqs.1156.
- Yoo, K., Weinman, B., Mudd, S.M., Hurst, M., Attal, M., and Maher, K., 2011, Evolution of hillslope soils: The geomorphic theater and the geochemical play: *Applied Geochemistry*, v. 26, no. SUPPL., doi: 10.1016/j.apgeochem.2011.03.054.

Appendix A: Workflow of GPS-assisted soil mapping at Garner Run

1. We generated white-to-black shaded relief map in ArcGIS of area to be mapped. We derived a slope map from 1 m lidar and color low slopes white and high slopes black. We would adjust range of colorbar to reflect targeted area: in the low-sloping bench, I would emphasize more subtle features, so black might correspond to a lower slope degree (15-20), whereas in the steeper hillslopes, the black point might be set to 30 or 40.
2. In Layout view, we generated a 20 m x 20 m grid to overlay the map (you can also display the UTM Easting and Northing along the margins). We laid out the map on the page such that each box is about 1 cm across when printed. This way, when we went into the field to map, each box can fit four mapping categories (we were mapping at 5 m resolution).
3. We saved the map as a PDF exactly how it was to be printed (Under “Export Map”, ensure that, under the “Advanced” tab, the “Export Map Georeferenced Information” box is checked).
4. We devised a numbering scheme for each soil cover.
 - 0 – exposed bedrock (BR)
 - 1 – open boulder field (OB)
 - 2 – canopied boulder field (BC)
 - 3 – boulder/soil mix (BS)
 - 4 – soil-mantled (SM)

We mapped very little **exposed bedrock** (BR) at the site, except in a small patch along the ridgeline Tussey Mountain. **Open boulder fields** (OB) were open to the sky above, with no trees growing within the field. Typically, boulders in open boulder fields were

white, shiny, and sharp-edged. **Canopied boulder fields** (BC) were patches of boulders with little to no interstitial soil, though trees would be growing within some of the boulders. We considered boulders to lack interstitial soil if they moved or wobbled when stepped on or kicked. Boulders would often be stacked atop each other with open air in between. These boulders could be white and pointy, but they could also be covered in lichen and have more rounded edges. **Boulder/soil mix** (BS) was defined as boulders stuck within interstitial soil; they did not wobble or move when stepped on or kicked. We considered the cover BS when a 5 meter roving window on the ground had 10%-66% boulders (greater than 66% boulders would be BC, and less than 10% boulders would be SM). **Soil-mantled** (SM) cover contained less than 10% boulders at the surface.

5. We uploaded the georeferenced PDF to a cloud service (like Box or Dropbox) accessible from a smartphone (if you're not concerned with saving the file, it's easy to save it as an email attachment and then open it in the smartphone). We used the Avenza PDF Maps application for the smartphone (<http://www.avenza.com/avenza-maps>), and when we selected the georeferenced PDF, we opened it with the PDF Maps app to load it into the Avenza Maps app. (You will see under the file name something to the effect of "no geospatial information" if, for some reason, your map is unreferenced. Double-check this before going out to the field!)
6. A typical smartphone's internal GPS has an accuracy between 10 and 15 m. For more precise mapping, we employed an external DGPS antenna (Eos Arrow 100: <http://www.eos-gnss.com/arrow-100/>) which typically achieved an accuracy of 3 m in the worst scenario and 0.5-1.0 m accuracy in the best scenario. We connected the smartphone to the antenna via Bluetooth and used the EosToolsPro app to monitor connection to

various GPS constellations and vertical and horizontal RMS. The coordinates displayed on Avenza Maps reflects the Arrow GPS-derived position, overriding the phone's internal GPS.

7. When we were field mapping, we had the map loaded up on the Avenza Maps app on the smartphone. In this way we could directly match our current location to the paper map corresponding to the georeferenced PDF. In each corner of the 20 x 20 m grid, we wrote the number corresponding to the soil category, thus ensuring coverage at 5 m resolution. We also drew in the orientation of the contact between two units as a line between the numbers. The benefit of mapping with numbers instead of colors allowed us to revise the map if you make an error. However, at the end of the day, we often found it useful to “color-by-number” to see patterns or areas we missed.
8. Before packing up for the day, we captured a photo of the map in case the paper map was misplaced. When we returned to campus we scanned the maps and saved them as image files to be imported into ArcMap.
9. We imported and georectified the scanned map images in ArcMap. We then mapped out the contacts between the soil units according to the DiBiase geologic mapping guide (<http://sites.psu.edu/dibiase/teaching/making-a-geologic-map-in-arcgis-10-x/>). The general workflow is to create a feature class “MapUnitPolys” populated with polygons of the various soil textures (with subtype code representing each cover type), as well as line features in feature classes “Contacts” and “MapBorders.” Map borders will make a box around the mapped area, and contacts will be digital traces of the contacts mapped in the field. After all contacts are drawn in, polygons representing the cover types are “filled in” by selecting the contacts (and, when applicable, map borders) that make up the boundary

of the cover type area and then selecting “construct.” Because we used these polygons to derive zonal statistics, it is important that polygons within or adjacent to other polygons are not simply overlapping, but that they are “cut out” of each other (i.e. one spot on the landscape does not have two cover types mapped upon it, even though one will display on top of the other).

Appendix B. Soil pit descriptions

Soil horizons were described using a standard NRCS pedon description form. Dry and moist colors were determined in the field according to the Munsell® soil color book. Where described, texture was determined by feel in the lab (modified from Thien 1979).

Profile A

07-10-2015

253113 E, 4509192 N

Soil-mantled, adjacent to boulder canopy in valley floor

0-34+ cm	O/A	Very clayey soil with boulders mixed in; Dense root assemblage in
	and B	first 10 cm or so

Profile B

07-10-2015

253082 E, 4509495 N

Steep; soil-mantled pit flanked by boulder patches

0-8 cm	O/A	<i>no description</i>
--------	-----	-----------------------

8-17 cm	E	<i>no description</i>
---------	---	-----------------------

17+ cm	B	sandy brownish yellow layer, fine-grained but still gritty. Very sandy to medium/coarse gravels
--------	---	---

Profile C

07-15-2015

253256 E, 4509418 N

On top of lobe and just uphill of toeslope boulder field

0-14 cm O/A *no description*

14-27+ cm E Crumbly, not clayey. Peds have roots. Rock at 27 cm.

Profile D

07-15-2015

252890 E, 4509329 N

Soil pit at the foot of boulders, soil-mantled

0-7 cm O/A *no description*

7-20+ cm B brown/red clayey soil

Profile E

07-29-2015

0243049 E, 4509342 N

Bouldery soil, Tussey side, valley floor

6-0 cm	O	crumbly w/ roots forming a mat, dry
0-3 cm	E	No rock fragments in E. Sparse root assemblage. 2-3 VF roots. Color: 7.5YR 5/3. Subrounded blocky peds, fine-medium. Wavy boundary
4-20+ cm	B	Varied spatial distribution of roots: some areas with 2-3 VF roots, others with 6-7 F roots. Rock fragments of quartzite, volumetrically less than 5%. 0-17 cm depth contains coarse, gravel-cobble sized fragments in a soil matrix. 17+ cm rock fragments cease to be seen in the observable horizon. Peds are coarse to very coarse in size, angular-subangular blocky. Color: 7.5YR 5/6. Lower boundary not observed

Profile F

07-30-15

252959 E, 4509424 N

Boulder canopy, steep Tussey Mountain side

4-0 cm	O	<i>no description</i>
0-6 cm	A	10YR 2/1 (10YR 2/1 moist), clear wavy boundary, sandy clay loam, many very fine/fine roots throughout. Very friable, slightly sticky, moderately plastic
6-13 cm	E	7.5 YR 6/2 (10YR 4/2 moist), clear wavy boundary, sandy clay loam. 60% subrounded quartzite cobbles. Some very fine/fine roots throughout. Friable, slightly sticky, moderately plastic

13-16 cm	B1	7.5 YR 3/3 (7.5 YR 4/3 moist), broken boundary, sandy clay loam. 60% subrounded quartzite coarse gravel to cobbles. Many very fine/fine roots throughout. Very friable, slightly sticky, moderately plastic
16-26+ cm	B2	7.5 YR 4/4 (7.5 YR 4/3 moist), broken boundary, sandy clay loam. 75% subrounded quartzite coarse gravel to cobbles. Some medium to coarse roots throughout. Friable, slightly sticky, moderately plastic. Lower boundary not observed (large boulder in the way)

Profile G

07-30-2015

253099 E, 4509233 N

Boulder canopy in valley floor. Angry ants.

4-0 cm	O	<i>no description</i>
0-7 cm	A	7.5 YR 2.5/1 (10YR 3/1 moist), clear wavy boundary, loam. 60% subangular quartzite cobbles. Many very fine to fine roots throughout, few medium roots throughout. Friable, slightly sticky, very plastic.
7-35+ cm	B	7.5 YR 4/4 (10 YR 5/4 moist), silty clay. From 7-30 cm, 60% subruonded quartzite cobbles; from 30+ cm, 20% subrounded coarse gravel. Many fine roots throughout, few coarse roots throughout. Firm, moderately sticky, very plastic.

Profile H

07-06-2016

4509481 N, 253359 E

- | | | |
|----------------|-----|---|
| +5 – 0 cm | O | Organic horizon; largely leaves with very fine to fine roots throughout. |
| 0 – 3 cm | O/A | Organic horizon; fewer roots, with some very fine sand grains |
| 3 – 16 cm | E | Sandy clay loam. 7.5YR 6/2 color (7.5YR 5/2 moist). Abrupt wavy boundary. Moderate sub-angular blocky structure, with dark organic stains on pedon surfaces. Few fine tubular pores. Common very fine to fine roots and few medium roots throughout. Abundant gravel to cobble size rock fragments. |
| 16 – 46+
cm | B | 7.5YR 3/4 color (5YR 3/4 moist), with 5YR 3/3 (5YR 2.5/2 moist) color mottles associated with weathering rinds on clasts. Gradual wavy boundary. Moderate granular structure. Common fine roots and few medium roots throughout. Few medium gravel to cobble size rock fragments throughout. |

Profile I

07-06-2016

4509583 N, 253175 E

- | | | |
|------------|---|-----------------|
| +14 – 0 cm | O | Organic horizon |
|------------|---|-----------------|

- | | | |
|-------------|---|--|
| 0 – 30 cm | E | 7.5YR 6/2 color (7.5YR 6/2 moist). Moderate sub-angular blocky structure, with 7.5YR 5/6 color pedons. Rocky boundary. Few to common coarse roots and common fine roots throughout. Few coarse and common fine dendritic tubular pores. Abundant sub-angular to sub-rounded medium gravel to cobble size rock fragments. |
| 30 - 47+ cm | B | Sandy clay loam. 10YR 5/6 color (10YR 4/4 moist). Moderate sub-angular blocky structure. Rocky, gradual irregular boundary. Few coarse roots, common medium roots, and few to common fine roots throughout. Few very fine tubular pores. Sub-angular to sub-rounded coarse gravel to cobble size rock fragments. |

Profile J

07-07-2016

253230 E, 4509297 N

Below lobe

- | | | |
|-----------|---|---|
| +3 – 0 cm | O | Organic horizon |
| 0 – 4 cm | E | 7.5YR 5/2 color (7.5YR 4/2 moist). Clear wavy boundary. Common fine roots and few medium roots throughout. Medium gravel to cobble fragment blocks. |

4 – 16+ cm B 10YR 6/6 color (10YR 5/6 moist). Common fine roots and few medium roots throughout. Medium gravel to cobble fragment blocks.

Profile K

7-7-2016

253354 E, 4509290 N

Just above lobe

+2 – 0 cm O Organic horizon

0 – 5 cm E Medium gravelly. 7.5YR 3/2 color (7.5YR 2.5/2 moist). Abrupt smooth boundary. Common fine roots throughout.

5 – 15+ cm B Medium gravelly to cobbly. 10YR 5/6 color (10YR 4/6 moist). Sub-angular blocky structure. Common fine roots and common coarse roots throughout.

S.J. Thien. 1979. *A flow diagram for teaching texture by feel analysis*. Journal of Agronomic Education. 8:54-55

Appendix C. Modeling Scenarios and Constants

Each model run was performed in a one-dimensional depth profile of a total of 6.5 m depth, with samples at 6.4, 4.8 and 3.4 m below the surface. The model domain is composed of a number of nodes (i) assigned certain depths below the surface between 0 and 6.5. Node spacing varies by model scenario (see below).

Total production with depth is calculated for each node i according to

$$P_{N i} = P_{N spall i} + P_{N muon i}, \quad (1)$$

where

$$P_{N spall i} = P_N(0) e^{-\rho_{sed} \frac{d_i}{\Lambda_{spall}}} \quad (2)$$

and

$$P_{N muon i} = P_N(0)_m e^{-\rho_{sed} \frac{d_i}{\Lambda_{muon}}}. \quad (3)$$

Production and decay are then calculated for each timestep Δt (here, always 500 year) according to

$$N_i^n = N_i^{n-1} e^{-\frac{\Delta t}{T_N}} + P_{N i} \Delta t e^{-\frac{\Delta t}{T_N}} \quad (4)$$

where N_i^n is the concentration of a nuclide at the current timestep at node i and N_i^{n-1} is the concentration of a nuclide at the previous timestep at node i , and $T_N = \frac{\lambda_N}{\log_2}$.

For our models we employ one value for the ratio between surface production of ^{26}Al and ^{10}Be , and a different value for the ratio of inherited ^{26}Al and ^{10}Be when material is buried in the valley. We found that slope material contained a $[\text{^{26}Al}]/[\text{^{10}Be}]$ value of 6.49 ± 0.49 . While the production of nuclides at the surface may be a higher number (more consistent with recent work) and our *in-situ* production of nuclides should reflect that, this value is an appropriate one to assign to material being buried in the valley. Thus, we will hold the inheritance ratio, R_{inh} , constant at 6.5 for each model run, and allow the production ratio, R_{prod} , to vary.

Constant	Explanation	Value chosen for model
$P_{10}(0)$	Spallation production of ^{10}Be at surface, in atoms/g/year	6.07
$P_{26}(0)$	Spallation production of ^{26}Al at surface, in atoms/g/year	$P_{10}(0) * R_{prod}$
$P_{10}(0)_m$	Muon production of ^{10}Be at surface, in atoms/g/year	0.09
$P_{26}(0)_m$	Muon production of ^{26}Al at surface, in atoms/g/year	0.834

Λ_{spall}	Attenuation length for spallation production, in g/cm^2	160
Λ_{muon}	Attenuation length for muon production, in g/cm^2	1000
λ_{10}	^{10}Be half-life, in years	1387000
Λ_{26}	^{26}Al half-life, in years	705000
ρ_{sed}	Sediment density, in g/cm^3	2

For the single-event deposition scenario (Fig. 8a), we modeled the evolution of [26Al] and [10Be] within a 6.5-m package of sediment with uniform inheritance. To simulate a range of burial ages, we used six total burial times – 50, 100, 150, 200, 300 and 400 kyrs – to track the evolution of the two nuclides, and calculated the final [26Al]/ [10Be] with depth. We calculated production, decay and total concentration of nuclides at nodes spaced 0.05 m apart. First, we set the initial concentration and ratio of 26Al and 10Be uniformly throughout the 6.5 m package. Second, we calculated the total production of 26Al and 10Be – both spallation and muon production – at each node. Then, we used a timestep of 500 years to iteratively calculate both the production and decay of nuclides in the sediment package until the model reached the predetermined total burial time.

For the steady accumulation scenario (Fig. 8b), we modeled the evolution of the nuclides in an increasingly thicker package of sediment until it reached a total thickness of 6.5 m. To simulate a range of initial sedimentation dates, we used six total accumulation times – 50, 100, 150, 200, 300 and 400 kyrs. In order to achieve the same final thickness for each of the total accumulation times, we varied the sediment accumulation rate. For example, in order to deposit 6.5 m in 50 kyrs, our sedimentation rate would be 0.13m per 1 kyr, whereas the oldest initial sedimentation at 400 kyrs would require 0.01625 m per 1 kyr. Because we use a constant timestep in each model run, our node spacing also changes with the variable accumulation times because each node reflects the thickness of sediment deposited at each timestep (in this case, our timestep is 500 years such that node spacing is 0.06 m for the fastest accumulation and 0.008 for the slowest accumulation).

In our steady accumulation scenario, at each timestep of 500 years, a package of sediment with a thickness of one node would be added to the top of the sediment package. This node would contain the initial concentration and ratio of 26Al and 10Be stated in our model constants. After this new node is added to the model domain, the total production with depth is re-calculated at each node to reflect the new depth profile. Then, we calculate both the production and decay of nuclides in the new depth profile. Once the entire packages' production and decay has been calculated, it iterates to the next timestep where a new node of sediment is added and the process begins again. The model repeats these steps until the entire 6.5 m package has accumulated.

For the pulsed deposition scenario (Fig. 8c), we used a scheme similar to that of the single-event deposition described above, with nodes spaced 0.05 m apart. However, we set two total burial times, one for the lower package (“valley floor time”) and one for the upper package (“time since pulse”). First, we set the initial concentration and ratio of 26Al and 10Be uniformly throughout the package encompassing both the lower and upper clast, along with some overlying fill. While we do not have any constraints on the depth at which the depositional hiatus occurred

because we have no samples between 4.8 and 3.4 m depth, the model outputs are not particularly sensitive to the difference between a hiatus surface between about 4.5 and 3.4 m depth. Like before, we calculate the production profile with depth and at each timestep iteratively calculate production and decay until the “valley floor time” has been reached.

After the valley floor time has been reached, the remainder of the sediment is deposited such that the total package thickness is 6.5 m. These nodes, which contain uniform initial ^{26}Al and ^{10}Be according to our model constants, are concatenated to the top of the existing nodes. Then, the production profile with depth is re-calculated to reflect the new depth profile, and at each timestep iteratively calculate production and decay until the “time since pulse” has been reached.

Appendix Tables

Table A1a: Soil horizon sampling by soil pit

TMMS		LRVF		LRMS		LRRT	
Depth (cm)	Horizon						
0-6	A	0-10	E	0-12	E	0-5	E
6-21	AE	10-14	Bhs	12-15	Bhs	5-7	Bhs
21-37	Bw1	14-20	Bs	15-26	Bs	7-14	Bs
37-75	Bw2	20-32	Bw1	26-50	Bw1	14-33	Bw1
75-95+	Bw3	32-65+	Bw2	50-72	Bw2	33-60	Bw2
				72-145	C	60-95	Bt
						95-138	BC
						138-155+	2Cr

Reproduced from Brantley et al. 2016

Table A1b: Cosmogenic nuclide analyses

Original data							
Sample ID	LLNL #	measured 10/9		blank correction		blank corrected 10/9	
573GR01	BE40804	7.99951E-13	1.14539E-14	1.2044E-15	6.561E-16	7.99E-13	1.15E-14
573GR02	BE40805	6.40918E-13	7.41656E-15	1.2044E-15	6.561E-16	6.40E-13	7.45E-15
573GR03	BE40806	9.61463E-13	1.65773E-14	1.2044E-15	6.561E-16	9.60E-13	1.66E-14
573GR04	BE40807	1.78695E-13	3.40176E-15	1.2044E-15	6.561E-16	1.77E-13	3.46E-15
573GR05	BE40808	4.97293E-13	6.55272E-15	1.2044E-15	6.561E-16	4.96E-13	6.59E-15
573GR06	BE40809	1.0192E-12	1.68187E-14	1.2044E-15	6.561E-16	1.02E-12	1.68E-14
573GR07	BE40811	4.12494E-13	1.00101E-14	1.2044E-15	6.561E-16	4.11E-13	1.00E-14
573GR08	BE40812	2.7867E-13	3.33365E-15	1.2044E-15	6.561E-16	2.77E-13	3.40E-15
573GR09	BE40813	8.43602E-13	9.57543E-15	1.2044E-15	6.561E-16	8.42E-13	9.60E-15
582GR10	BE41286	1.19365E-12	1.99956E-14	1.2044E-15	6.561E-16	1.19E-12	2.00E-14
582GR11	BE41287	5.27532E-13	1.00178E-14	1.2044E-15	6.561E-16	5.26E-13	1.00E-14
583GR12	BE41288	1.55992E-12	3.37879E-14	1.2044E-15	6.561E-16	1.56E-12	3.38E-14
573BLK	BE40815	5.95935E-16	2.9184E-16				
582BLK	BE41284	1.11777E-15	1.5333E-16				
583BLK	BE41297	1.89953E-15	2.24865E-16				
	<i>average</i>	<i>1.20E-15</i>	<i>6.56E-16</i>				
Sample ID	PRIME #	measured 26/27		blank correction		blank corrected 26/27	
573GR07	201602926	3.33E-13	1.41E-14	1.97E-14	9.76E-15	3.13E-13	1.72E-14
573GR08	201602927	5.31E-13	2.40E-14	1.97E-14	9.76E-15	5.11E-13	2.59E-14
573GR09	201602928	1.38E-12	3.43E-14	1.97E-14	9.76E-15	1.36E-12	3.57E-14
582GR10	201602963	2.23E-12	5.45E-14	1.97E-14	9.76E-15	2.21E-12	5.54E-14
582GR11	201602964	4.21E-13	1.55E-14	1.97E-14	9.76E-15	4.02E-13	1.83E-14
583GR12	201602967	2.05E-12	4.75E-14	1.97E-14	9.76E-15	2.03E-12	4.85E-14
573BLK	201602929	28.49	6.70	2.8E-14	5.7E-15		

582BLK	201602965	21.32	5.73	2.1E-14	7.2E-15
583BLK	201602968	9.18	7.21	9.2E-15	0.0E+00
			<i>average</i>	<i>1.97E-14</i>	<i>9.76E-15</i>

Replicate data

Sample ID	LLNL #	measured 10/9		blank correction		blank corrected 10/9	
591BLK	BE42470	1.19E-15	1.95E-16				
591GR08	BE42472	1.90E-13	2.60E-15	1.19E-15	1.95E-16	1.89E-13	2.61E-15
591GR10	BE42476	5.27E-13	6.34E-15	1.19E-15	1.95E-16	5.25E-13	6.34E-15

Sample ID	PRIME #	measured 26/27		blank correction		blank corrected 26/27	
591BLK	201700661	2.49E-15	1.90E-15				
591GR08	201700662	4.37E-13	1.31E-14	2.49E-15	1.90E-15	4.34E-13	1.32E-14
591GR10	201700666	1.44E-12	3.17E-14	2.49E-15	1.90E-15	1.44E-12	3.18E-14

Table A2: Point count locations and results

Site label	Easting	Northing	D ₅₀	D _{min}	D _{max}	D ₁₆	D ₈₄	Cover type	Field label
TMOB1	252743	4509567	43	20	132	28	69	Open boulder field	openb_ptct1
TMOB2	253015	4509661	45	16	124	28	70	Open boulder field	openb_ptct2
TMOB3	252810	4509520	30	14	79	20	44	Open boulder field	openb_ptct6
TMOB4	252977	4509547	26	10	65	19	37	Open boulder field	openb_ptct4
TMOB5	252985	4509480	29	11	102	21	43	Open boulder field	openb_ptct5
LRBC1	253474	4508925	31	12	72	21	42	Canopied boulder field	bcanopy_ptct8
LRBC2	253186	4508836	35	13	115	23	56	Canopied boulder field	bcanopy_ptct1
LRBC3	253149	4508944	34	14	105	21	53	Canopied boulder field	bcanopy_ptct2
LRBC4	253095	4509035	22	9	60	15	32	Canopied boulder field	bcanopy_ptct3
TMBC1	252800	4509558	28	10	103	18	44	Canopied boulder field	bcanopy_ptct6
TMBC2	253052	4509500	29	10	62	19	40	Canopied boulder field	bcanopy_ptct7
TMBC3	252898	4509414	25	11	52	17	35	Canopied boulder field	bcanopy_ptct5
TMBC4	253082	4509415	26	10	59	17	35	Canopied boulder field	bcanopy_ptct4
TMBS1	252808	4509625	20	12	57	16	30	Boulder/soil mix	bsoil_ptct3
TMBS2	252967	4509232	23	12	57	17	30	Boulder/soil mix	bsoil_ptct1
TMBS3	253032	4509165	22	11	66	15	27	Boulder/soil mix	bsoil_ptct2
TMBS4	253213	4509256	23	10	77	16	33	Boulder/soil mix	bsoil_ptct4
LRBS1	253324	4508936	28	10	57	19	35	Boulder/soil mix	bsoil_ptct5
LRBS2	253295	4509027	23	12	47	15	28	Boulder/soil mix	bsoil_ptct6
LRBS3	253186	4509091	18	7	47	14	26	Boulder/soil mix	bsoil_ptct7
GPC01	253258	4509216	12	f	41	1.0	21	Channel	GPC01
GPC02	253188	4509148	15	f	66	0.8	27	Channel	GPC02
GPC03	253111	4509082	20	f	73	1.9	33	Channel	GPC03
GCP04	253030	4509032	13	f	59	1.5	25	Channel	GCP04
GPC05	248083	4505270	9.8	f	45	5.4	16	Channel	GPC05
GPC06	248129	4504988	9.3	f	58	1.5	23	Channel	GPC06
GPC07	250023	4506728	8.5	f	26	3.3	15	Channel	GPC07
GPC08	249550	4506569	5.7	f	30	f	12	Channel	GPC08

D₁₆, D₅₀ and D₈₄ refer to the 16th, 50th and 84th percentile of intermediate grain axis measurements, in cm. D_{min} and D_{max} refer to the minimum and maximum intermediate grain size observed, in cm.

f = fine (< 0.2 cm)

Appendix Figures

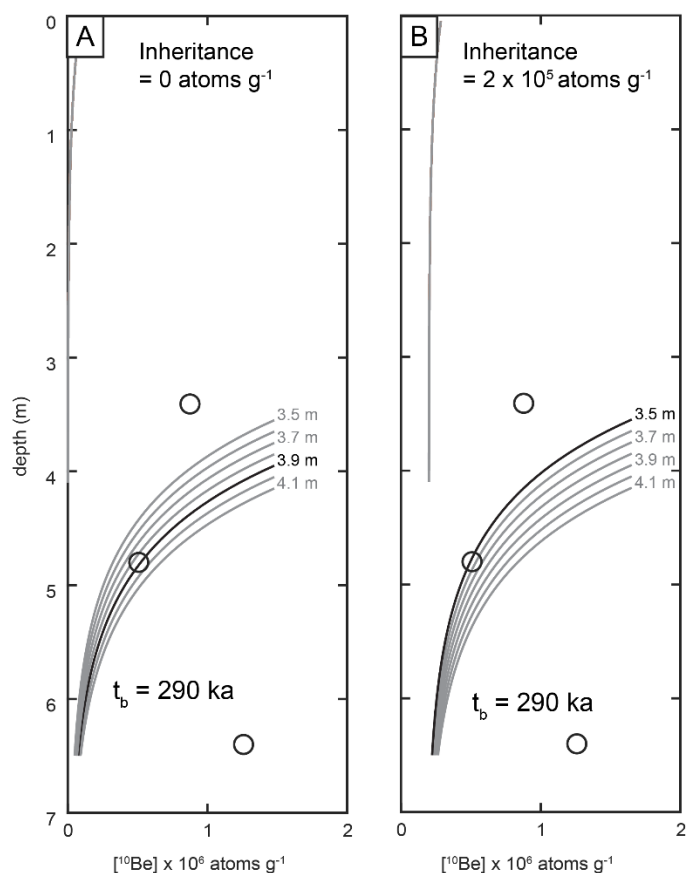


Fig. A1: Constraining the depth of the hiatus surface using the absolute concentration of ^{10}Be in the middle clast. (A) Given the best-fitting burial age of 290 ka, the middle clast at 4.8 m depth would have needed to have been shielded by some fill in order to maintain its modern-day concentration. Given 0 inherited ^{10}Be , the lowest the hiatus could have occurred is at 3.9 m depth (a depth closer to the middle clast would have resulted in too much dosing). (B) Given the shallowest hiatus surface at 3.5 (just below the top clast), the maximum inheritance allowed for the middle grain is $2 \times 10^5 \text{ atoms g}^{-1}$.

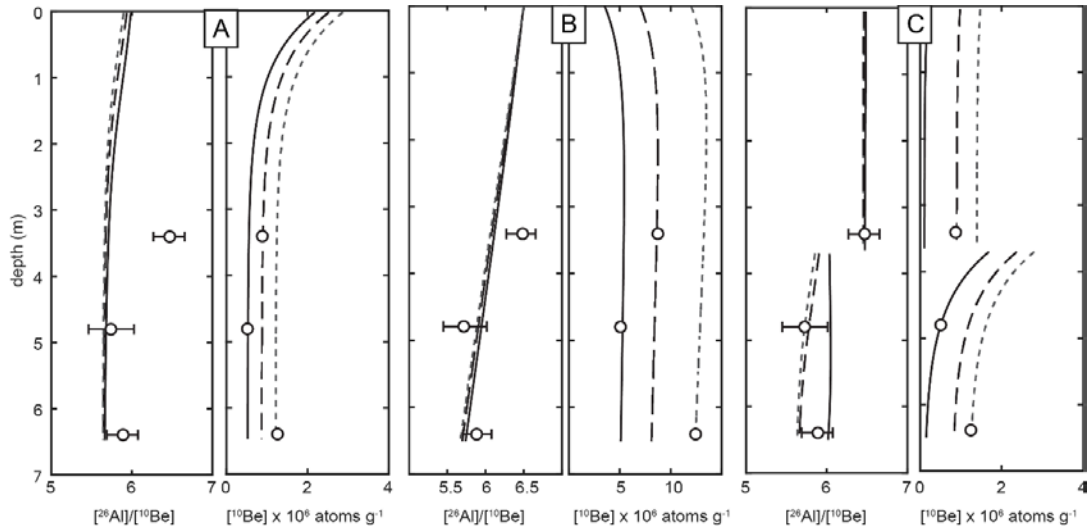


Fig. A2: The effect of the range in possible inheritance of buried grains on $[^{26}\text{Al}]/[^{10}\text{Be}]$ for burial age of 290 ka. Each forward model is run three times with an inheritance to match each grain's modern $[^{10}\text{Be}]$. (A) In the single depositional event scenario, inherited concentrations of ^{10}Be do not result in significant variability of $[^{26}\text{Al}]/[^{10}\text{Be}]$, particularly at the depths of our samples. (B) In the steady accumulation scenario, inherited concentrations of ^{10}Be also do not result in significant variability of $[^{26}\text{Al}]/[^{10}\text{Be}]$, particularly at the depths of our samples. (C) The relatively low concentration of ^{10}Be exhibited by the middle clast results in a curve shape that is very different from the curve produced by higher initial concentrations. However, this curve is still within the range of error for the lower two samples.

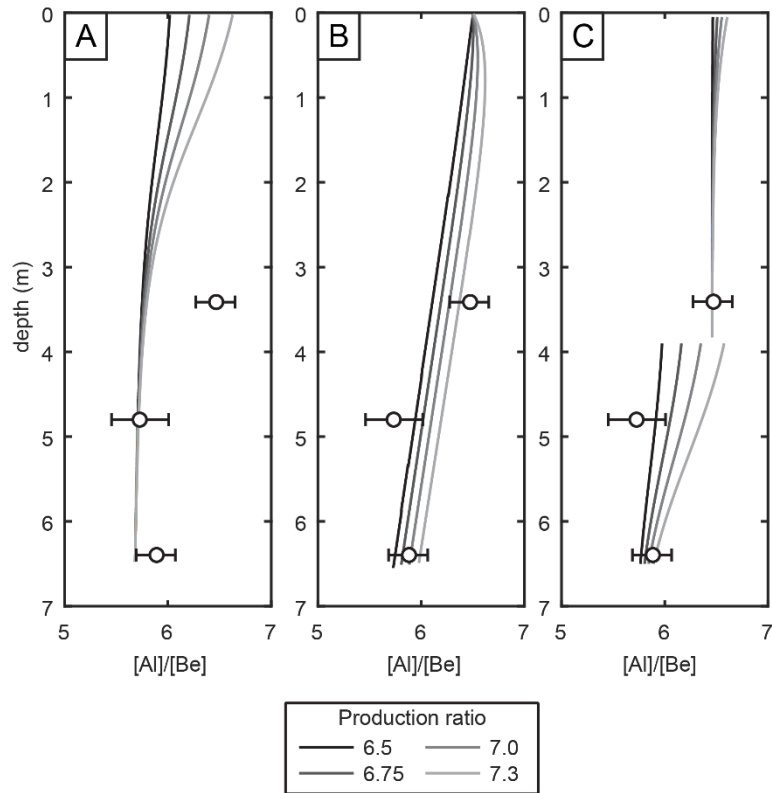


Fig. A3: The effect of a range in possible surface production ratios on $[^{26}\text{Al}]/[^{10}\text{Be}]$ for burial age of 290 ka with an inherited $[^{26}\text{Al}]/[^{10}\text{Be}]$ of 6.5. (A) In the single depositional event scenario, the range of surface production ratios do not result in significant variability of $[^{26}\text{Al}]/[^{10}\text{Be}]$, particularly at the depths of our samples. (B) The range of surface production ratios do not produce trends that fit our data. (C) At higher surface production ratios, it becomes difficult to reconcile the ratio of the middle clast with the ratio of the lower clast. Overall, a higher surface production ratio results in older burial times for our samples.